AGU PUBLICATIONS

JGR

Journal of Geophysical Research: Atmospheres

RESEARCH ARTICLE
10.1002/2014JD022931

Key Points:
- Atmospheric refractivity profiles found using Airborne Radio Occultation (ARO)
- This is the first utilization of ARO in a full-scale science mission
- ARO refractivity is generally within 2% of independent sounding measurements

Correspondence to:
B. J. Murphy,
bmurphy@purdue.edu

Citation:
Murphy, B. J., J. S. Haase, P. Muradyan, J. L. Garrison, and K.-N. Wang (2015), Airborne GPS radio occultation refractivity profiles observed in tropical storm environments, *J. Geophys. Res. Atmos.*, *120*, 1690–1709, doi:10.1002/2014JD022931.

Received 1 DEC 2014
Accepted 30 JAN 2015
Accepted article online 3 FEB 2015
Published online 6 MAR 2015

Airborne GPS radio occultation refractivity profiles observed in tropical storm environments

B. J. Murphy[1], J. S. Haase[2], P. Muradyan[1], J. L. Garrison[3], and K.-N. Wang[3]

[1]Department of Earth, Atmospheric and Planetary Sciences, Purdue University, West Lafayette, Indiana, USA, [2]Scripps Institution of Oceanography, University of California, San Diego, La Jolla, California, USA, [3]Aeronautics and Astronautics Engineering, Purdue University, West Lafayette, Indiana, USA

Abstract Airborne GPS radio occultation (ARO) data have been collected during the 2010 PRE-Depression Investigation of Cloud systems in the Tropics (PREDICT) experiment. GPS signals received by the airborne Global Navigation Satellite System Instrument System for Multistatic and Occultation Sensing (GISMOS) are used to retrieve vertical profiles of refractivity in the neutral atmosphere. The system includes a conventional geodetic GPS receiver component for straightforward validation of the analysis method in the middle to upper troposphere, and a high-sample rate (10 MHz) GPS recorder for postprocessing complex signals that probe the lower troposphere. The results from the geodetic receivers are presented here. The retrieved ARO profiles consistently agree within ~2% of refractivity profiles calculated from the European Center for Medium-Range Weather Forecasting model Interim reanalyses as well as from nearby dropsondes and radiosondes. Changes in refractivity obtained from ARO data over the 5 days leading to the genesis of tropical storm Karl are consistent with moistening in the vicinity of the storm center. An open-loop tracking method was implemented in a test case to analyze GPS signals from the GISMOS 10 MHz recording system for comparison with geodetic receiver data. The open-loop mode successfully tracked ~2 km deeper into the troposphere than the conventional receiver and can also track rising occultations, illustrating the benefit from the high-rate recording system. Accurate refractivity retrievals are an important first step toward the future goal of assimilating moisture profiles to improve forecasting of developing storms using this new GPS occultation technique.

1. Introduction

Radio occultation (RO) is a remote sensing technique for measuring atmospheric properties using Global Navigation Satellite System (GNSS) signals. It provides high-resolution vertical soundings that have low sensitivity to clouds and precipitation, making them appealing for assimilation in numerical weather prediction (NWP) models [*Poli et al.*, 2008, 2010; *Schreiner et al.*, 2007]. The RO technique measures the excess phase delay and Doppler shift of a GNSS radio signal which results from the atmospheric refraction of the signal along the path between the transmitting GNSS satellite and a receiver in Low Earth Orbit (LEO) [*Kursinski et al.*, 1997]. The airborne RO technique is an extension of the spaceborne technique, which we review below.

Atmospheric refractivity in the neutral atmosphere is related to temperature, air pressure, and water vapor pressure by equation (1):

$$N = \frac{k_1 P}{T} + \frac{(k_2 - k_1)e}{T} + \frac{k_3 e}{T^2}; N = (n-1)\times 10^6 \quad (1)$$

where N is refractivity in N units, P is atmospheric pressure in hPa, e is water vapor pressure in hPa, T is temperature in Kelvin, and n is the index of refraction [*Healy*, 2011; *Smith and Weintraub*, 1953]. The constant coefficients, $k_1 = 77.6$ hPa^{-1}; $k_2 = 70.4$ K hPa^{-1}; $k_3 = 3.739\times 10^5$ K^2 hPa^{-1}, are derived from empirical data [*Bevis et al.*, 1994]. The refractive bending angle of the signal raypaths through the atmosphere can be determined from the excess Doppler and the positions and velocities of the receiver and transmitter using geometric optics [*Fjeldbo et al.*, 1971; *Vorob'ev and Krasil'nikova*, 1994]. A vertical profile of refractivity is then calculated from the bending angles using an Abel transform [*Hajj et al.*, 2002; *Kursinski et al.*, 1997].

In the lower troposphere, multipath propagation occurs due to sharp gradients in refractivity principally due to large moisture variations. The superposition of signals with different Doppler frequencies corresponding to multiple raypaths interferes with the receiver tracking of the signal and retrieval of bending angle using

geometric optics. Radio holographic methods have been developed to analyze signal phase and amplitude using Fourier operators, such as Full Spectrum Inversion (FSI), to determine the bending angle profile in the presence of multipath [*Gorbunov*, 2002; *Gorbunov and Lauritsen*, 2004; *Jensen et al*., 2003, 2004].

Once the refractivity profile is determined, it can be used to infer temperature and humidity [*Hajj et al*., 2002; *Healy and Eyre*, 2000; *Rodgers*, 1976]. When using a receiver in LEO, a vertical resolution of ~1.4 km in the stratosphere to less than 500 m near the Earth's surface can be achieved when using geometric optics, corresponding to the first Fresnel zone for GPS RO [*Healy and Eyre*, 2000; *Kursinski et al*., 1997]. The resolution when using a radio holographic method is approximately 100 m in the lower troposphere with higher resolutions theoretically possible [*Gorbunov et al*., 2004; *Jin*, 2013]. Vertical resolutions in the lower stratosphere estimated at 100–200 m have been obtained using the FSI method [*Tsuda et al*., 2011].

The first GPS RO mission, the GPS/MET (Global Positioning System/Meteorology) experiment, was launched in 1995 and successfully demonstrated the GPS RO concept [*Ware et al*., 1996]. Since the GPS/MET experiment, multiple spaceborne programs have obtained radio occultation measurements using on board GPS receivers, such as the German CHAllenging Minisatellite Payload (CHAMP) satellite [*Wickert et al*., 2001], US-Taiwan cooperative Constellation Observing System for Meteorology Ionosphere and Climate (COSMIC)/Formosa Satellite 3 [*Anthes et al*., 2008], International Satelite de Aplicaciones Cientifico-C (SAC-C) [*Hajj et al*., 2004], National Aeronautics and Space Administration (NASA) Gravity Recovery and Climate Experiment [*Anthes*, 2011; *Wickert et al*., 2009], and European Meteorological operational (Metop) [*von Engeln et al*., 2011] satellites.

With the success of spaceborne systems, it was proposed that the RO technique be adopted for use with a receiver inside the Earth's atmosphere either stationed on a mountaintop [*Zuffada et al*., 1999], or on board an aircraft [*Healy et al*., 2002; *Lesne et al*., 2002; *Xie et al*., 2008]. Airborne radio occultation (ARO) makes it possible to target regions of interest providing an increased number of observations within a time frame relevant for synoptic scale storm development, as opposed to spaceborne RO where the sampling is constrained by the orbits of the available LEO satellites and therefore is relatively sparse. ARO complements dropsondes and other airborne remote sensing techniques in that the limb-soundings sample the larger-scale environment to the sides of the flight path and can be made at a safe distance from dangerous deep convection within storm systems.

We developed the GNSS Instrument System for Multistatic and Occultation Sensing (GISMOS) for ARO measurements as well as reflection measurements for ocean surface roughness, wind speed, salinity, and surface soil moisture [*Garrison et al*., 2007; *Voo et al*., 2009]. The GISMOS system was tested in 2008 using the National Science Foundation (NSF) Gulfstream V (GV) research aircraft at flight altitudes of approximately 14 km over the southeastern United States [*Lulich et al*., 2010; *Muradyan*, 2009, 2012]. The proof of concept was demonstrated [*Haase et al*., 2014] in a preliminary analysis of the data from the 2010 PRE-Depression Investigation of Cloud systems in the Tropics (PREDICT) field campaign to study developing tropical storms [*Montgomery et al*., 2012]. The focus of this paper is an extension of the work of *Haase et al*. [2014] to a statistical analysis of the ARO results from the complete conventional geodetic GPS receiver data set during PREDICT and a preliminary assessment of the utility of the measurements for studying the tropical storm environment. It includes extensive comparisons with dropsonde and radiosonde data as well as NWP model analyses. Previous studies have demonstrated the ability of spaceborne GPS RO to measure the global characteristics of mature tropical cyclone temperature structure and to provide novel approaches for determining tropical cyclone cloud top heights and their empirical relation to storm intensity [*Biondi et al*., 2011, 2013; *Vergados et al*., 2013, 2014]. The motivation for this work is to provide additional data for assimilation into numerical models to improve forecasts [*Haase et al*., 2012]. Previous case studies have indicated that the assimilation of COSMIC spaceborne RO is beneficial to numerical forecasts of tropical cyclones [*Chen et al*., 2009; *Huang et al*., 2010; *Liu et al*., 2012]. However, these studies included only a limited number of profiles within 1200 km of the cyclone center. This work leads the way for future studies of the open-loop analysis of the GISMOS 10 MHz data where the ARO technique will be able to provide 10–14 profiles near the cyclone center per day.

Section 2 reviews the motivation and background for the PREDICT campaign, and provides a description of the GISMOS system and its use during the campaign. We implemented a geometric ray optics retrieval method for the analysis of the data from the conventional geodetic receivers for the upper part of the troposphere,

which we describe in section 3. Section 4 presents an assessment of the accuracy of the ARO results through comparisons with dropsondes, radiosondes, and numerical weather model reanalysis profiles. The consistency of the refractivity variations with environmental moisture variations in the vicinity of the developing storm Karl is also examined in section 4. A preliminary analysis of the GISMOS 10 MHz GNSS Recording System (GRS) data, which will allow much more comprehensive sampling of the storm regions for rising as well as setting occultations, and will sample into the middle to lower troposphere, is given in section 5.

2. PREDICT Campaign

2.1. Campaign Objectives

The PREDICT experiment took place from 15 August 2010 until 30 September 2010 and was based at St. Croix, U.S. Virgin Islands. It has been postulated that the presence of a dynamically protected region of convection and vorticity comoving with a tropical wave could lead to an area of enhanced moisture favorable for cyclogenesis [*Dunkerton et al.*, 2009]. Testing this hypothesis was addressed by the PREDICT experiment in the Caribbean and western Atlantic [*Evans et al.*, 2012; *Montgomery et al.*, 2012]. During PREDICT, airborne missions were flown to investigate the developing tropical cyclone environment before the disturbances reached tropical storm strength. The missions were planned to provide observations within the axes of the African Easterly waves. Approximately 50% of minor Atlantic hurricanes, Saffir-Simpson category 1 and 2, and over 80% of intense Atlantic hurricanes, category 3 and above, develop from an African easterly wave [*Landsea*, 1993]. However, determining which waves will develop is a challenge.

The location of the closed circulation region was predicted to be near the intersection of the critical line, where the wave speed matches the mean flow and the axis of the wave trough [*Dunkerton et al.*, 2009; *Wang et al.*, 2009]. On a given pressure surface, the critical line was typically oriented east-west, whereas the axis of the wave trough was typically oriented north-south. During PREDICT, a well-defined circulation about this point of intersection combined with enhanced total column water vapor in the forecast models motivated a mission. Dropsonde sampling of the area of circulation was used to evaluate the conditions that distinguished between developing and nondeveloping cases [*Davis and Ahijevych*, 2012; *Komaromi*, 2013].

The primary objective of this study is to provide a preliminary assessment of the ARO method accuracy using the rich PREDICT dropsonde data set and to develop an ARO data set for future assimilation with associated observation error estimates. Although dropsonde and radiosonde profiles have their own associated errors, they are currently the best independent benchmark for accuracy relative to other observation systems and are often used for validation of remote sensing systems. Radiosonde biases originate from instrumental error, manufacturer type, and radiation heating. However, these biases have been extensively studied to determine corrections and quality control for many of these effects [*Durre et al.*, 2005; *Moradi et al.*, 2013; *Reale et al.*, 2012; *Sun et al.*, 2013]. Dropsonde instrumentation is comparable to radiosonde, and we expect similar error characteristics. *Wang et al.* [2009] and *Wang* [2005] found good agreement between radiosonde and dropsonde relative humidity and temperature measurements in the lower troposphere (surface to 5 km altitude) where the mean difference was typically less than 2% in relative humidity and ~0.4°C in temperature, based on 71 colocated radiosonde and dropsonde data [*Wang*, 2005]. We therefore define agreement with these soundings as an assessment of ARO profile accuracy, with the caveat that the observations have fundamentally different spatial characteristics [*Kuo et al.*, 2004]. The expected theoretical error for ARO refractivity is expected to be better than 0.5% up to about 1 km below aircraft height given a velocity accuracy of the navigation system of 5 mm/s or better [*Muradyan et al.*, 2010]. However, if the line of sight for the ARO geometry crosses strong horizontal gradients of refractivity, the assumption of spherical symmetry can introduce refractivity biases up to 1% in the upper troposphere increasing to a maximum of ~4.5% below 3 km altitude [*Xie et al.*, 2008]. This has motivated development of a nonlocal observation operator to account for lateral variations when radio occultation data are assimilated [*Liu et al.*, 2008; *Ma et al.*, 2009; *Sokolovskiy et al.*, 2005a, 2005b].

2.2. Campaign Measurements

The National Science Foundation (NSF) GV research jet was deployed for 26 research missions studying eight storm systems during the campaign. Dropsondes were deployed on all research flights to measure atmospheric conditions in the environment of each storm. Over 500 dropsondes were deployed during the campaign [*Montgomery et al.*, 2012]. The GISMOS ARO system was also deployed on the GV and sampled

the survey area during all missions. Twenty-one ARO refractivity profiles were retrieved from the conventional geodetic receiver system over the 26 missions for this study, of which nine were from flights into a tropical disturbance which ultimately developed into Hurricane Karl and were studied extensively during PREDICT. Six flights were made into the pre-Karl disturbance over 5 days from 10 to 14 September 2010. The disturbance was investigated from early in its development through its genesis to a tropical storm, which made this an ideal system to assess the characteristics of ARO refractivity profiles in the moisture environment of a developing tropical system.

GISMOS recorded occultation data from four geodetic quality dual-frequency Trimble NetRS GPS receivers as well as a 10 MHz GNSS Recording System (GRS). Two high-gain antennas, with the gain patterns focused on the horizon for extra sensitivity in tracking occulting satellites, were mounted on the sides of the fuselage. Two GPS avionic antennas were also mounted on each side of the aircraft. Each of the four geodetic receivers recorded 5 Hz data from one of the side antennas. A GPS inertial navigation system provided high-accuracy aircraft position and velocity using another GPS avionic antenna installed on top of the GV fuselage. The GRS recorded one channel from each of the high-gain side looking antennas and one channel from the top antenna. A common timing signal for each receiver was provided by a Symmetricom ET6000 GPS timing receiver with an ovenized crystal oscillator with stability of 3×10^{-11} over 1 s. Flight level in situ measurements of temperature were made at 50 Hz with a fast response, all weather, de-iced avionics sensor (Rosemount Model 102AL TAT) with 0.5°C accuracy (http://www.hiaper.ucar.edu/handbook/index.html). In situ pressure was measured at flight level with 0.1 hPa accuracy. Humidity measurements were made with a vertical cavity surface emitting laser hygrometer and a Buck research model 1011c hygrometer (Project managers' data quality report at https://www.eol.ucar.edu/content/predict-aircraft-documentation-summary). However, because of the inconsistency of recording accuracy, these humidity data were not used.

The precise position and velocity of the aircraft were calculated with the Applanix Mobile Mapping Suite postprocessing software [*Mostafa et al*., 2001] using a tightly coupled Kalman filter solution combining 10 Hz GPS observations and 200 Hz inertial measurement unit (IMU) observations. Precise final orbits and clocks were used from the International GNSS Service (IGS) [*Beutler et al*., 1999, 2009]. Forward and reverse Kalman filter precise point positioning solutions were averaged to provide a combined solution including optimal error corrections to the linear acceleration and angular rates measured by the IMU. The position precision is better than 6 cm in the horizontal and 90 cm in the vertical, and velocity precision is better than 5 mm/s velocity in all components, as required for accurate airborne retrievals, contributing to less than 0.5% refractivity error [*Muradyan et al*., 2010; *Xie et al*., 2008].

3. Retrieval Method and Data Analysis

3.1. GPS Observations of Excess Phase

The travel time of the signal observed by a GPS receiver is a function of the speed of propagation, which depends on the refractive index of the atmosphere, integrated along the path length. The deviation of the latter from a straight line also depends on the refractive index. The gradient of refractivity causes bending of the GPS signals along the propagation path. The tangent point of the refracted raypath is the point of the closest approach to the Earth's surface as shown in Figure 1. The observable for ARO is given in terms of the total carrier phase in meters, ϕ, of the GPS signal shown in equation (2),

$$\Phi_R^T = D_R^T + cC^T + cC_R + I_R^T + cG + \phi_R^T + M_R^T + \varepsilon \tag{2}$$

where D_R^T is the vacuum straight line geometric distance in meters between the transmitting GPS satellite and the GPS receiver on board the aircraft, c is the speed of light in meters per second, cC^T and cC_R are the satellite and receiver clock errors, respectively, I_R^T is the error due to the ionosphere, cG is the relativistic time correction to compensate for the eccentricity of GPS satellite orbits, M_R^T is the integer ambiguity of the carrier wave at the start of signal tracking, ϕ_R^T is the excess phase delay caused by refraction in the neutral atmosphere, and ε is the measurement error including thermal noise and local multipath. The superscript T refers to the transmitting GPS satellite, and the subscript R refers to the receiving aircraft.

Excess phase was found by subtracting the satellite clock error (provided with the IGS orbits), the relativistic effect, the geometric distance, and the ionosphere correction from the total phase observed for the satellite.

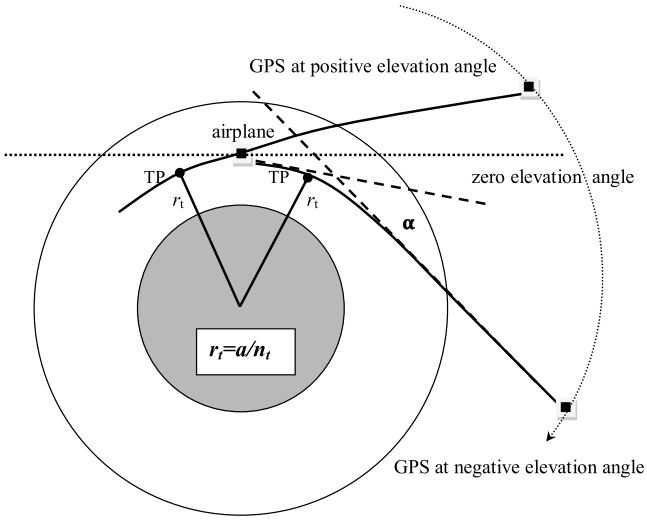

Figure 1. An occulting GPS satellite shown at positive and negative elevation angle relative to the local horizon of the aircraft. The radius vector to the tangent point, r_t, is the point of closest approach of the raypath to the surface of the Earth, and α is the bending angle due to refraction. The index of refraction at the tangent point is n_t, and the impact parameter is $a_t = n_t r_t$.

The ionosphere correction was obtained from the ionosphere free total phase using the L1 and L2 GPS signals from the GISMOS dual-frequency geodetic receivers [*Misra and Enge*, 2006] as shown in equation (3).

$$I_R^T = \frac{f_{L1}^2}{f_{L1}^2 - f_{L2}^2}\phi_{L1} - \frac{f_{L2}^2}{f_{L1}^2 - f_{L2}^2}\phi_{L2} \quad (3)$$

Higher-order corrections for ionospheric effects are neglected. The excess Doppler, f_d, was found by taking the time derivative of the excess phase, which removes the unknown integer ambiguity.

$$f_d(\mathrm{m/s}) = \frac{\mathrm{d}}{\mathrm{d}t}\left\{\phi_{\mathrm{R}}^T + C_{\mathrm{R}} \cdot c + \varepsilon\right\} \quad (4)$$

The excess Doppler was smoothed with a second-order Savitzky-Golay filter [*Schafer*, 2011] with a span of 5 s to reduce the amount of noise propagated through further analysis of the data. The window size of the filter was chosen to preserve the expected vertical resolution at the tangent point defined by the first Fresnel zone of the ray [*Xie et al.*, 2008]. In order to remove the receiver clock error, cC_{R}, the smoothed Doppler from a GPS satellite at a high elevation, where tropospheric effects were assumed to be negligible compared to other error sources, was subtracted from the occulting satellite Doppler, as shown in Figure 2.

3.2. Refractive Bending Angle

The impact parameter, a, of the occulting signal raypath is the product of the tangent point radius from the Earth's center and the refractive index at that point (Figure 1). The impact parameter is constant along the raypath when refractivity is spherically symmetric. When spherical symmetry is assumed, the bending angle of the signal raypath, α, as a function of impact parameter can be determined from the excess Doppler, given the relative positions and velocities of the satellite and aircraft [*Vorob'ev and Krasil'nikova*, 1994]. The excess Doppler shift of the GPS signal from transmitter to receiver is given by equation (5) [*Hajj et al.*, 2002; *Melbourne*, 2005].

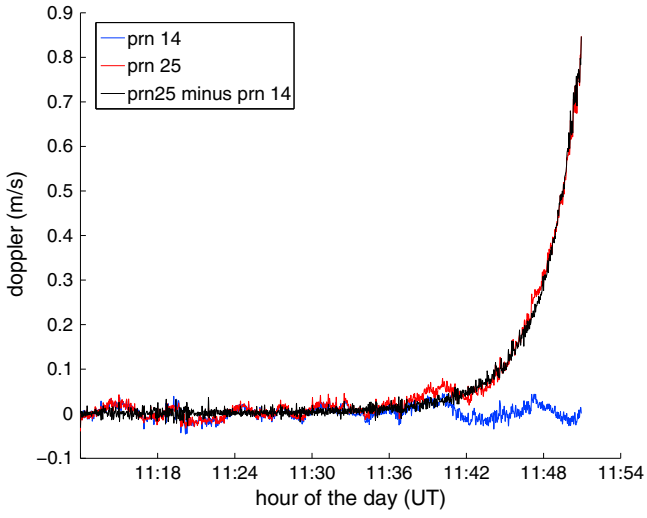

Figure 2. The excess Doppler shift (observed minus straight line vacuum path) is shown for the occulting satellite PRN25 (red) during RF18 and high elevation satellite PRN14 (blue) for the same flight. The difference, PRN25 minus PRN14 (black), is taken to remove the variation due to the receiver clock error. At later times, the raypath samples deeper in the atmosphere producing a greater Doppler shift. [From *Haase et al.*, 2014].

$$f_d = \frac{1}{\lambda}\left[n_{\mathrm{T}}\mathbf{k}_{\mathrm{T}} \cdot \mathbf{v}_{\mathrm{T}} - n_{\mathrm{R}}\mathbf{k}_{\mathrm{R}} \cdot \mathbf{v}_{\mathrm{R}} - \mathbf{k} \cdot (\mathbf{v}_{\mathrm{T}} - \mathbf{v}_{\mathrm{R}})\right] \quad (5)$$

The terms $\mathbf{v}_{\mathrm{R}}$ and $\mathbf{v}_{\mathrm{T}}$ are the aircraft and satellite vector velocities, $\mathbf{k}$ is the unit vector in the straight line direction from transmitter to receiver, while $\mathbf{k}_{\mathrm{T}}$ and $\mathbf{k}_{\mathrm{R}}$ are the unit vectors in the directions of signal departure from the transmitter and subsequent arrival at the receiver, respectively. The refractive index of the

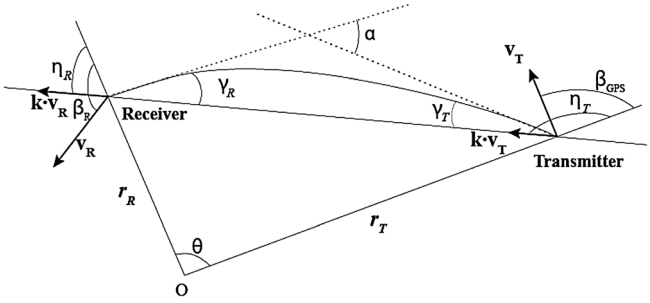

Figure 3. The geometry of the airborne receiver and GPS satellite in the occultation plane containing the center of Earth curvature, the aircraft, and satellite. The tangents to the signal raypath at the source and receiver define the total bending angle, α, which provides information on the refractivity of the atmosphere. Subscript T refers to the GPS satellite transmitter and subscript R refers to the aircraft GPS receiver. The satellite and airplane velocities are labeled by $\mathbf{v}_T$ and $\mathbf{v}_R$, respectively. This illustration defines the angles used in equation (6).

atmosphere at the location of the aircraft and the satellite is n_R and n_T, respectively. The dot products in equation (5) can be evaluated to express the excess Doppler shift in terms of the scalar velocities and angles in the plane containing the aircraft, satellite, and Earth center as shown in Figure 3 and given in equation (6) [*Vorob'ev and Krasil'nikova*, 1994].

$$f_d = \frac{v_T}{\lambda}[\sin(\eta_T - \beta_T)\sin\gamma_T + (\cos\gamma_T - 1)\cos(\eta_T - \beta_T)] - v_R[n_R\sin(\beta_R - \eta_R)\sin\gamma_R + (n_R\cos\gamma_R - 1)\cos(\beta_R - \eta_R)] \tag{6}$$

For the airborne geometry, the satellite is at an elevation where refractivity is negligible and the transmitter index of refraction, n_T, is unity. The in situ flight level data were used to calculate the refractive index, n_R, at the aircraft using equation (1). Because in situ flight level, water vapor measurements were not functioning reliably during PREDICT, the refractivity at the aircraft flight level was calculated with only the first pressure term using the mean value of the flight level pressure and temperature over the duration of the occultation. The contribution of the wet components to total refractivity is small relative to other error sources at the typical GV flight altitude of 14 km, ~0.05% of total refractivity [*Muradyan*, 2009]. The bending angle, α, is the sum of the two unknown angles in equation (6):

$$\alpha = \gamma_R + \gamma_T \tag{7}$$

A second equation in these variables can be derived from Bouguer's formula [*Born and Wolf*, 1999]

$$a = r_T \sin(\gamma_T - \eta_T) = n_R r_R \sin(\gamma_R + \eta_R) = \text{constant} \tag{8}$$

where r is the radial distance from the center of curvature to a point on the raypath. Note that equations (6) and (8) differ from those described in *Kursinski et al.* [1997], and the spaceborne radio occultation literature because $n_R r_R$ is explicitly included and n_R is not assumed to be unity. Equations (6) and (8) were solved iteratively using successive substitution to find γ_R and γ_T, where γ_T is expected to be small and is initially chosen to be equal to zero. To compensate for the oblateness of the Earth, the local spherical radius and center of curvature at the tangent point were calculated and the coordinates and velocities were transformed into the reference frame with its origin at the center of curvature prior to the calculation of the bending angle [*Syndergaard*, 1998].

For the setting occultations, the GPS satellite was observed beginning above the horizon of the aircraft (positive elevation angle) and continued below the horizon (negative elevation angle) until tracking was lost, as illustrated in Figure 1. For every raypath below the horizon of the aircraft, there is a raypath above the horizon with the same impact parameter, a [*Healy et al.*, 2002; *Zuffada et al.*, 1999]. The maximum impact parameter occurs at zero-elevation angle relative to the local aircraft horizon. The bending angle of the raypath increases slowly as the setting satellite moves from above the aircraft horizon to zero-elevation angle. The bending angle then increases much more rapidly as the satellite sets below the horizon, as seen in Figure 4.

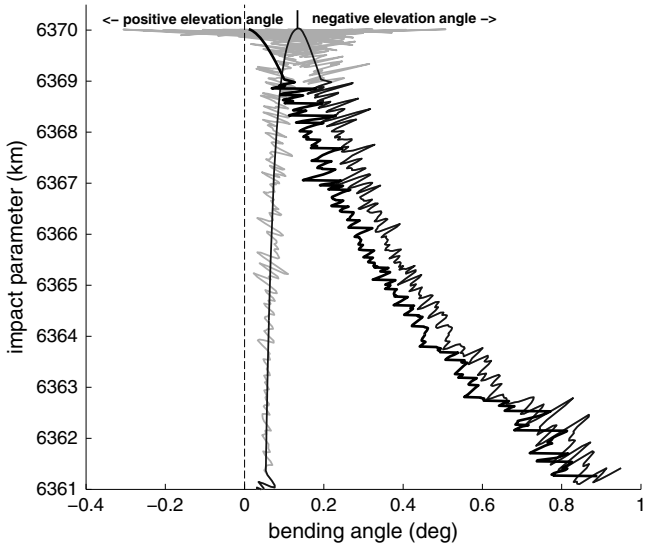

Figure 4. The bending angle from the occultation of satellite PRN25 during RF18 on 13 September 2010 (gray). Superimposed is the bending angle profile with the noisy section near zero-elevation angle and the positive elevation angles replaced with simulated values from an initial estimate of the refractivity profile (darker gray). The partial bending angle is shown in black.

3.3. Refractivity Retrieval

The bending angle, α, in a spherically symmetric atmosphere is an integral function of the refractive index as a function of radius, r, from the center of curvature [*Hajj et al.*, 2002; *Kursinski et al.*, 1997].

$$\alpha = -a\int_{r_t}^{r_R} \frac{1}{\sqrt{n^2r^2 - a^2}} \frac{\mathrm{d}(\ln n)}{\mathrm{d}r}\,\mathrm{d}r - a\int_{r_t}^{r_T} \frac{1}{\sqrt{n^2r^2 - a^2}} \frac{\mathrm{d}(\ln n)}{\mathrm{d}r}\,\mathrm{d}r \quad (9)$$

The radius at the tangent point is r_t, and the integration continues to r_R (the radius at the receiver) and r_T (the GPS transmitter radius) in the left and right terms, respectively. In spaceborne RO with both the receiver and transmitter outside the atmosphere, there is no bending accumulated in the vacuum from radius of the low earth orbiting satellite receiver to the radius of the GPS satellite, so the two terms are equivalent. When the receiver is inside the atmosphere as for the airborne case, these two terms are not equivalent. However, the bending angle for a negative elevation angle raypath can be expressed as a sum of the bending angle accumulated below the radius of the aircraft and the bending accumulated from the radius of the aircraft to the radius of the GPS satellite.

$$\alpha = -2a\int_{r_t}^{r_R} \frac{1}{\sqrt{n^2r^2 - a^2}} \frac{\mathrm{d}(\ln n)}{\mathrm{d}r}\mathrm{d}r - a\int_{r_R}^{r_T} \frac{1}{\sqrt{n^2r^2 - a^2}} \frac{\mathrm{d}(\ln n)}{\mathrm{d}r}\mathrm{d}r \quad (10)$$

The second term is equivalent to the bending accumulated for a positive elevation angle ray with equivalent impact parameter. The partial bending angle, α', is defined as the difference between the bending angles of positive and negative elevation angle rays [*Xie et al.*, 2008]

$$\alpha' = \alpha_N - \alpha_P = -2a\int_{r_t}^{r_R} \frac{1}{\sqrt{n^2r^2 - a^2}} \frac{\mathrm{d}(\ln n)}{\mathrm{d}r}\mathrm{d}r \quad (11)$$

and depends only on the atmospheric refractivity below the aircraft. The refractive index at a specific height in the atmosphere below the receiver is found using the Abel inverse of equation (11)

$$n(a) = n_R \exp\left[\frac{1}{\pi}\int_{x=a}^{x=n_R r_R} \frac{\alpha'(a)}{\sqrt{x^2 - a^2}}\mathrm{d}x\right] \quad (12)$$

where $x = nr$. Once again, equation (12) differs from that describing the spaceborne case by the factor n_R. The Abel transform pair given by equations (11) and (12) can be used to either make a forward calculation of partial bending angle from a known refractivity profile or an inverse calculation of refractivity from a profile of partial bending angle.

As an example, the bending angle found from the excess Doppler measured during an occultation of satellite PRN25 (GPS satellites are identified by the Pseudorandom Number code) during research flight 18 (RF18) on 13 September 2010 is shown in Figure 4. To find the partial bending angle, the point with maximum impact parameter in the ARO bending profile is found. This point is taken as zero-elevation angle, and the profile is split into positive and negative elevation angle sections. The positive and negative elevation bending angle sections were then each interpolated at equal impact parameter intervals of 0.01 km so that the partial bending difference could be formed. The noise in the excess Doppler profile produces

noise in the bending angle profile, which is greatest at zero-elevation angle. To reduce the propagation of this noise in the calculation of refractivity, the retrieval process was carried out in two steps. First, a refractivity profile was derived from the Abel inverse transform of the noisy partial bending angle profile. Then a quadratic fit was made to the log of refractivity as a function of height below the aircraft. The refractivity was extrapolated upward to 30 km height using an exponential function with a 7 km scale height. Assuming this smooth refractivity profile, the bending angle was simulated with a forward Abel calculation from equation (11). The noisy section of the bending angle profile near the maximum impact parameter and the positive elevation angle section of the bending angle profile were then replaced with the simulated bending angle profile, as shown in Figure 4. Because the refractivity at the aircraft height is constrained by the in situ measurement, the error made by extrapolating refractivity above the aircraft is small, and will be assumed to be insignificant compared to the bending angle noise that was eliminated. A revised partial bending angle was calculated and used in a second iteration of the inverse Abel transform to find the final estimate of the refractivity profile.

For comparison to the ARO refractivity profiles, we use equation (1) to calculate vertical refractivity profiles from dropsonde data as well as model reanalyses estimates of geopotential height, pressure, temperature, and relative humidity. Saturation vapor pressure was calculated from temperature following the Federal Meteorological Handbook No. 3 (www.ofcm.gov/homepage/text/pubs.htm). The geopotential height values in the dropsonde and model profiles, which are referenced to the equipotential surface at sea level, were converted to geometric height [*Hofmann-Wellenhof and Moritz*, 2006]. Then the geometric height was corrected for the difference between the geoid (sea level) and the WGS84 ellipsoid that serves as reference for the GPS geometric height using the EGM2008 geoid model [*Pavlis et al*., 2012] (www.geographiclib.sourceforge.net/cgi-bin/GeoidEval).

4. Results

We assessed the accuracy of ARO refractivity profiles by comparing them with dropsonde, radiosonde, and model reanalysis profiles at nearby locations. The location of the raypath tangent point moves horizontally with changing tangent point altitude as the receiver-transmitter geometry changes, primarily because the GPS satellite is moving significantly faster than the aircraft. To provide a consistent reference point for comparison, the ARO refractivity profile was assigned a location at the *occultation point*, which we defined as the tangent point location at 500 hPa, the height which approximately divides the mass of the atmosphere in half, or the lowest tangent point location if the profile does not extend below 500 hPa. Typically, the horizontal movement is on the order of 150–400 km. However, the drift is not linear in tangent point altitude, as shown in Figure 5. The drift is greatest at higher altitudes. The horizontal drift of the tangent point altitudes from 14 to 10 km was approximately twice the horizontal drift in the height interval from 10 to 6 km (Figure 5).

For each retrieved ARO profile, we selected the closest dropsonde profile for comparison. The maximum separation was 370 km. This relatively large distance criterion was chosen to provide a reasonable number of matches and is comparable to the criterion chosen in previous RO studies [*Sun et al*., 2010].

Dropsonde and ARO profiles were interpolated to common levels, and the difference between the ARO and the dropsonde profile was found using equation (13).

$$\delta_N = \frac{N_{\mathrm{ARO}} - N_{\mathrm{DROP}}}{N_{\mathrm{DROP}}} \times 100\% \tag{13}$$

The same approach was used for the model reanalyses. Because of the horizontal drift of the tangent point and the physical drift of the dropsonde descent, some differences are expected between ARO and the nearly vertical dropsonde profiles. In addition, horizontal gradients of refractivity along the signal raypath, especially due to smaller-scale moisture variations, limit the accuracy of the spherical symmetry assumptions used in the refractivity retrieval. The ARO retrieval represents a weighted average of the refractivity along the line of sight between the receiver and the satellite. The values are highly weighted toward the locations of the tangent points because that is where the density is greatest. For example, we used ray tracing to calculate in a 1-D atmosphere that 70% of the bending is accumulated within ±50 km of the tangent point at 10 km height and within ±170 km of the tangent point at 3 km height.

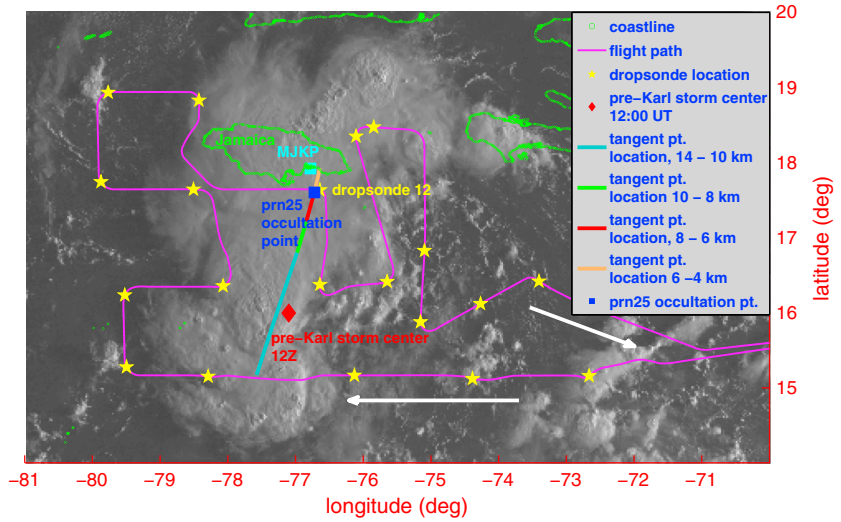

Figure 5. The RF18 flight path on 13 September 2010 (magenta) south of Jamaica superimposed on GOES-13 11:45 UT visible imagery. The yellow stars mark the deployed dropsondes. The tangent point drift for the occultation of GPS PRN25 is shown in cyan to orange. The horizontal tangent point drift rate becomes progressively smaller at lower heights. The pre-Karl storm center (red diamond) is shown south of Jamaica approximately 24 h before developing into a tropical depression and then tropical storm over the northwest Caribbean Sea on 14 September 2010.

4.1. Dropsonde and Radiosonde Comparison

We analyzed the GPS ARO data for 21 occultations recorded by the GISMOS geodetic receivers over the course of the campaign. Many more occultations were recorded by the GRS, and refractivity profiles will be retrieved from these data in future work. The ARO refractivity profiles extended from the aircraft height (typically about 14 km), until tracking was lost. The deepest profile was retrieved from the occultation of PRN25 satellite from flight RF18, Figure 5, which extended down to a height of 4.1 km. All of the ARO refractivity profiles extend from the aircraft altitude to at least 7.7 km altitude, and the average height reached for all profiles was 6.3 km. Figure 6b shows the refractivity profile from the RF18 PRN25 occultation, as well as the profile calculated from the dropsonde nearest to the occultation point (D20100913_132359

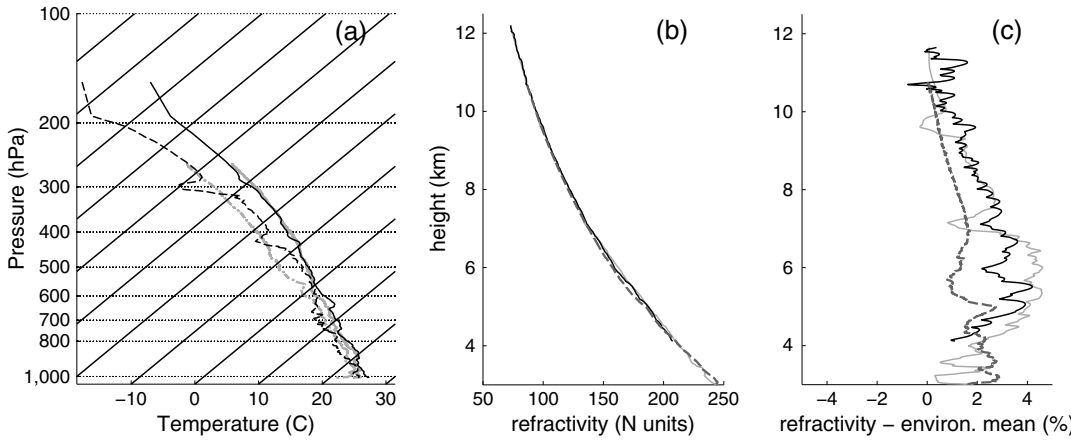

Figure 6. (a) The dewpoint (dashed) and temperature (solid) profiles measured by the nearby dropsonde (black) and radiosonde 12:00 UT MKJP (gray) on 13 September 2010. (b) Refractivity profiles derived using the PRN25 occultation data from RF18 (black), radiosonde MKJP (dashed), and dropsonde (gray). (c) The difference relative to the environmental mean of the ARO (black), radiosonde (dashed), and dropsonde (gray) refractivity. ARO differs by about 1% from the dropsonde over the height of the profile. ARO agrees well with the dropsonde, and both indicate high moisture relative to the environmental mean.

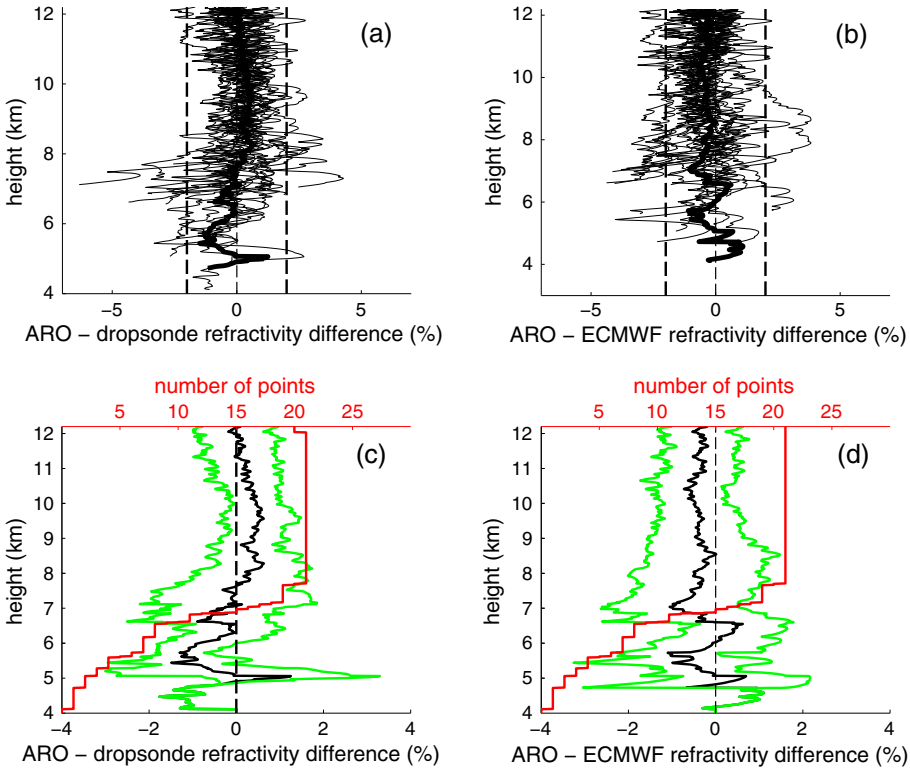

Figure 7. (a) Percent difference of RO refractivity profiles from dropsonde refractivity profiles (see equation (13)). In all panels, the mean is shown in bold black. The mean difference between RO and dropsondes is less than 1% for heights where the number of observations (red) is greater than 15. (b) Percent difference of RO refractivity profiles from the refractivity profile at the nearest ECMWF Interim reanalysis grid point. (c) The mean (black) and standard deviation (green) of RO-dropsonde refractivity and the number of observations (red) are shown at each height. (d) The mean (black) and standard deviation (green) of RO minus ERAI refractivity and the number of observations at each height (red). The standard deviation is less than 2% for all heights where the number of observations is greater than 15, roughly above 7 km.

from RF18 on 13 September 2010) (http://data.eol.ucar.edu/master_list/?project=PREDICT), and the profile calculated from the 12:00 UT Kingston (MKJP), WMO station #78397, radiosonde. For this case, the ARO refractivity differs from the dropsonde by about 1% over the height range of the profile, and both ARO and dropsonde refractivity (Figure 6c) are significantly higher than the environmental mean defined later in section 4.3. Both the ARO and dropsonde profiles sample air that is moister than the MKJP radiosonde profile (Figure 6a). The contribution of temperature versus moisture in these comparisons is discussed in detail in section 4.3.

Each of the ARO refractivity profiles was compared to the dropsonde deployed nearest to the occultation point, and the percent differences are shown in Figure 7a along with the mean of all profiles at each height. In Figure 7c the standard deviation is shown in green, and the number of profiles at each height is indicated in red. Below 7 km the sample size was too small to make a robust estimate, but the data are shown in Figure 7 to illustrate the penetration depth of observations below that height by the geodetic receivers. The average spatial separation between dropsonde and ARO occultation point was 118 km, and the greatest separation was 367 km. Fourteen of the 21 ARO profiles were within 120 km of a dropsonde location. The average temporal separation between the ARO profiles and the corresponding dropsonde release times was 1.42 h with 14 of the 21 profiles separated by less than 2 h. No attempt was made to distinguish between profiles in different convective environments. All flights were made when deep convection was present, and almost all missions were flown into storms before they reached tropical storm stage [*Montgomery et al.*, 2012].

The mean difference of ARO minus dropsonde refractivity is near zero at 12 km, increasing to 0.8% at 9.3 km and decreasing to zero at 8 km, with a positive bias (ARO higher than dropsonde refractivity). The mean difference shows a negative bias below 8 km. The standard deviation as a function of height is about 0.8% in the 12 km to 8 km height range, and then increases to 1% from 8 to 7 km. A 0.8% refractivity difference corresponds

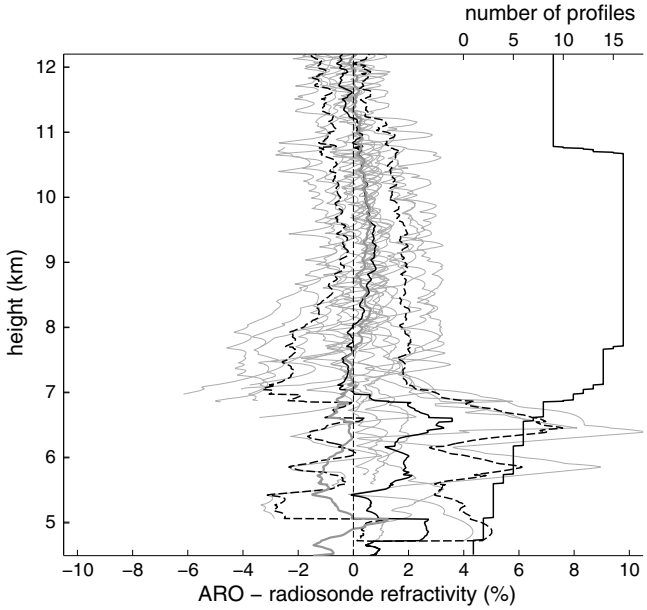

Figure 8. Refractivity difference between ARO and radiosonde profiles for all flights (gray). The mean difference (black) is less than 1% above 7 km where there are more than 10 profiles. The mean follows closely the mean difference from the ARO and dropsonde comparison, which is also shown (bold gray). The standard deviation (dashed black) increases from 1% at 12 km to 2% at 7 km. The number of profiles used in the mean for each height is shown on the right (black).

to a 2 K error in temperature at 10 km height, assuming temperature is about −34°C and refractivity is 95 N units at this height.

The ARO profiles were also compared with radiosonde profiles over the entire PREDICT campaign (Figure 8). Due to the sparseness of radiosonde stations in the Caribbean, the comparison was limited to 16 profiles that were within 400 km and 5.5 h spatial and temporal separation, and many of these pairs occurred on the ferry part of the flight or well away from the center of most active convection. The mean difference is near zero at 12 km, increasing to a maximum of 0.8% at 9.3 km, and decreasing back toward zero at 7 km as shown in bold in Figure 8. The ARO-radiosonde difference has similar height dependence as the ARO-dropsonde difference. The standard deviation over this height range increases from about 0.5% at 12 km to 2% at 7 km as shown in Figure 8, somewhat greater than the dropsonde because of the greater spatial and temporal separation.

Given the novelty of these results, it is useful to review similar studies with spaceborne RO. The ARO profile accuracy is comparable but a little lower than spaceborne RO profiles, as expected, by the level of noise introduced by the less stable platform. Available spaceborne RO profiles are too sparse for comparison to nearest ARO geodetic receiver profiles from PREDICT. However, we can evaluate the results relative to previous studies comparing spaceborne RO refractivity profiles with radiosonde soundings [*Kuo et al.*, 2005; *Sun et al.*, 2010; *Wickert et al.*, 2004; *Xu et al.*, 2009]. For instance, *Kuo et al.* [2005] compared spaceborne RO refractivity soundings from the NASA-German cooperative CHAMP mission with data from regional groups of radiosondes released within 2 h and 300 km of CHAMP RO soundings, comparable time and distance separation to our ARO-dropsonde comparisons. Similar to the airborne ARO-dropsonde comparison, CHAMP soundings at similar latitudes as PREDICT campaign also showed the mean difference increasing as the height decreased. The CHAMP-radiosonde refractivity bias in the Australia region varied from near zero to 0.5% in the height range of 12 to 4 km, and then decreased to negative values below 4 km, whereas in Figures 7c and 8, the ARO bias transitions to negative values below 8 km. The standard deviation of spaceborne RO also increases with decreasing height in a manner similar to the airborne case. For example, spaceborne RO gives a standard deviation of about 1% above 7 km, which increases to 4% at 4 km for 366 radiosonde comparisons from Australia in *Kuo et al.* [2005]. The ARO-dropsonde differences would be expected to be greater than spaceborne radiosonde, as well as terminating at higher levels, given that they were recorded in the challenging environment of the Caribbean region, always in proximity of storm systems. Despite these differences, it is encouraging to find initial results to be of comparable magnitude to results seen in the comparison of operational spaceborne RO soundings to radiosondes.

An extensive study with globally aggregated COSMIC spaceborne RO data [*Sun et al.*, 2010] revealed a refractivity bias of radiosondes under 0.2% from 12 to 6 km, and a standard deviation that increased from 0.7% at 12 km to 1.5% at 6 km. With a larger data set, that study also investigated the dependence of the standard deviation on spatial and temporal separation of the soundings from the spaceborne RO profiles. For 0–0.25 h separation at 7.5 km height, the standard deviation increases from 0.5% to 1.2% as the separation distance increases from 0 to 275 km. Thus, the ARO standard deviations are within the expected range, given the proximity to the soundings.

4.2. Model Analysis Comparison

The ARO refractivity profiles were also compared to refractivity profiles calculated using the European Center for Medium-Range Weather Forecasts (ECMWF) European Reanalysis Interim (ERAI) model [*Dee et al*., 2011]. The refractivity profiles were calculated from the pressure, temperature, moisture, and geopotential height values extracted from the model at the grid points nearest to the ARO occultation point for the comparison. The model values at 37 levels were interpolated to 0.75° resolution from 1.5°, but no time interpolation in the 6 h reanalysis was made as the ARO profiles were already well colocated in time with an average separation in time of 1.2 h. The temporal separation has less impact than spatial separation, as *Chen et al*. [2011] showed no variation in COSMIC RO agreement with model forecasts for 0–2.5 h separation. The average distance between ARO occultation points and the nearest model grid point was 30.6 km. Figure 7b shows the difference with ERAI as a function of height for each of the 21 ARO refractivity profiles and the mean difference at each height in bold. In contrast to the dropsonde comparison, the mean difference between ARO and ERAI is negative, from about −0.5% at 12 km to 7 km height to −1% at 7 km height. In Figure 7d, the number of profiles available at each height is shown in red, the mean difference again in black, and the standard deviation in green. The standard deviation is 1.5% in the 12 km to 9 km height range, increasing to 2% by 7 km height. The agreement with the independent dropsonde observations is slightly better than the agreement with the model.

The PREDICT campaign took place at tropical latitudes of 17–19°. An intercomparison among CHAMP and SAC-C spaceborne RO data and model fields [*Kuo et al*., 2004] illustrated the strong latitude dependence of the agreement among data sets. Moisture variability of the tropical lower troposphere causes larger standard deviations than observed at higher latitudes. The ECMWF Tropical Ocean and Global Atmosphere (TOGA) analysis at 2.5° resolution was used for that globally aggregated study. A bias of less than 0.2% was seen between spaceborne RO and ECMWF-TOGA in the 7–12 km height range for tropical latitudes with a standard deviation of about 0.5–1%. However, the standard deviation reached 3% near the surface in the tropics compared to less than 2% at latitudes greater than 30°. A comparison between the GNSS Receiver for Atmospheric Sounding (GRAS) spaceborne RO data and the ECMWF analysis also considered the latitude dependence [*Zus et al*., 2011]. For tropical latitudes from −30° to 30°, the standard deviation of GRAS RO refractivity differences increased from about 0.5% at 10 km to 2% at 6 km, comparable to the ARO statistics. The GRAS profiles also showed higher biases in the tropics of −3% at 1 km, compared to −1.5% biases at high latitudes. The PREDICT ARO model comparison statistics are thus more comparable to the spaceborne RO model statistics found in the tropics. In addition, the selective sampling of the ARO profiles in the vicinity of tropical storms contributes to larger differences relative to spaceborne RO that sampled the entire tropical latitude band, with a proportionally lower sampling of this highly variable tropical storm environment. This contributes to the larger standard deviations seen in Figures 7 and 8.

4.3. Pre-Karl Refractivity

A subset of the ARO profiles was used to examine refractivity structure as the pre-Karl system developed. In particular, we present the profiles retrieved near the National Hurricane Center (NHC) best track locations of the investigated area during the transition from tropical disturbance to tropical storm, relative to the surrounding environment. The pre-Karl disturbance first developed from the merger of a tropical wave and a low-pressure trough north of the South American coast just east of Venezuela on 1 September 2010. The disturbance moved west-northwest over the next 2 weeks into the Caribbean. Beginning on 10 September 2010, PREDICT flights RF14–RF19 were flown into the pre-Karl system over a 5 day period ending on the fourteenth (Figure 10). Over this period, pre-Karl development was slow and convection disorganized. Up until the thirteenth, the low-level circulation was displaced relative to the midlevel circulation [*Davis and Ahijevych*, 2012]. After the alignment of the circulations on the thirteenth, the disturbance developed further, reaching tropical storm strength on 14 September (day T-0). After this, Karl eventually moved west across the Yucatan Peninsula south of Cancun and developed into a major hurricane in the Bay of Campeche by 17 September (A detailed report is found at www.nhc.noaa.gov/pdf/TCR-AL132010_Karl.pdf).

In general, for developing disturbances observed during PREDICT, a warm core formed within 24 h of genesis with a temperature anomaly of up to 2 K in the upper troposphere near the storm center [*Komaromi*, 2013]. The daily mean temperature increased near the storm by about 3 K at 9 km altitude for pre-Karl flights over 10–14 September [*Smith and Montgomery*, 2012]. The observed warm core is consistent with previous studies of

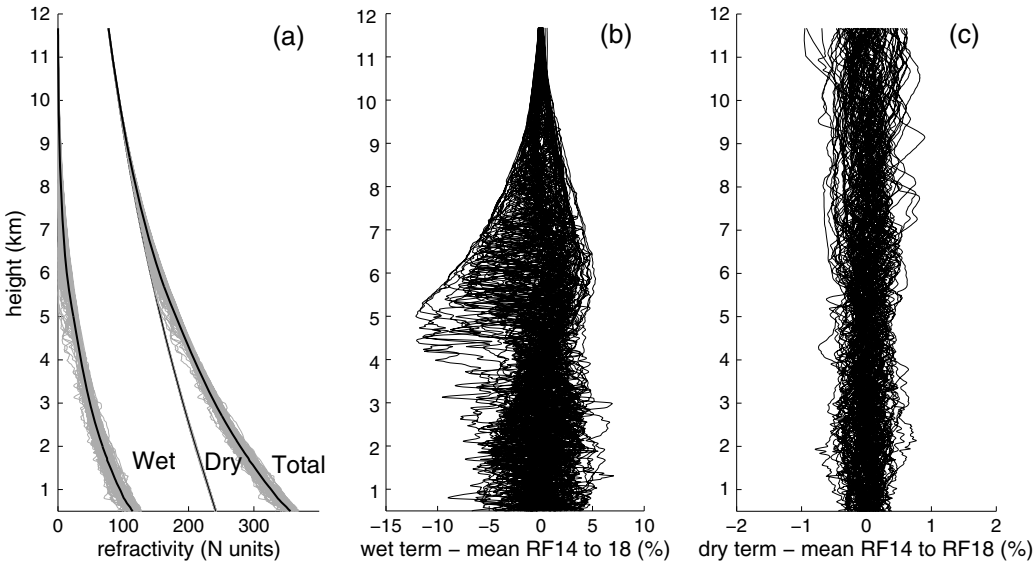

Figure 9. (a) The dropsonde pre-Karl environmental mean dry refractivity, total refractivity, and wet refractivity were calculated using all 105 PREDICT dropsondes from Karl flights RF14–RF18 over 10–13 September 2010. The pre-Karl environmental mean profile (black) is superimposed on all 105 profiles. (b) Variation of dropsonde wet refractivity relative to total refractivity (see equation (15)). (c) Variation of dropsonde dry refractivity relative to total refractivity. Even at 9.4 km, wet refractivity variations (sd 0.9%) measured by dropsondes are more than 3 times the dry variations (sd 0.3%).

tropical cyclones [*Biondi et al.*, 2013; *Davis et al.*, 2014; *Houze et al.*, 2009; *Kidder et al.*, 2000; *Merrill*, 1991]. The mean system relative humidity remained relatively constant below about 3 km over 10–14 September, while humidity generally increased in the midlevel to 10 km [*Smith and Montgomery*, 2012]. We investigate the variability in refractivity as seen in the dropsonde data over this time period and then examine the consistency of the ARO refractivity with the evolution of Karl as described in these previous studies.

The mean environmental refractivity over the 4 day period 10–13 September was calculated using data from all 105 PREDICT dropsondes deployed during RF14 through RF18 (Figure 9a). This mean refractivity profile, which we refer to as the pre-Karl environmental mean, provides a convenient pregenesis reference for comparison to profiles obtained with ARO data.

Atmospheric refractivity can be considered as the sum of a dry term that depends on temperature and dry pressure alone, and a wet term that contains water vapor pressure as shown by the rearrangement of equation (1) where dry pressure is equal to $P - e$.

$$N_{\text{dry}} = k_1 \frac{P-e}{T}; N_{\text{wet}} = k_2 \frac{e}{T} + k_3 \frac{e}{T^2} \tag{14}$$

In the upper troposphere where moisture levels are low, the dry term is dominant and most of the variations in refractivity are due to temperature variations. The wet component begins to make a greater contribution to refractivity variations below 9.4 km where moisture levels are greater (Figure 9b). On average, the wet contribution to the dropsonde refractivity is about 30–35% of total refractivity near the surface while just 0.3% of total refractivity at 12 km for the pre-Karl environmental mean profile. However, there is a significant difference between the magnitude of variations for the two components. Figure 9c shows the difference between the dry component calculated from each individual dropsonde and the pre-Karl environmental mean total refractivity using equation (15).

$$\delta N_i^{\text{dry}} = \frac{N_i^{\text{dry}} - \overline{N^{\text{dry}}}}{\overline{N^{\text{total}}}}; \quad \delta N_i^{\text{wet}} = \frac{N_i^{\text{wet}} - \overline{N^{\text{wet}}}}{\overline{N^{\text{total}}}} \tag{15}$$

The dry dropsonde refractivity varies at most by 0.5% from the mean over the five flights (RF14 through RF18). The difference between the wet component of refractivity for each dropsonde and the pre-Karl environmental mean total refractivity over the same period is shown in Figure 9b. The variation ranges from 3 to 10% with large variations in the 4–6 km height interval. Even at 9.4 km the standard deviation of the moist

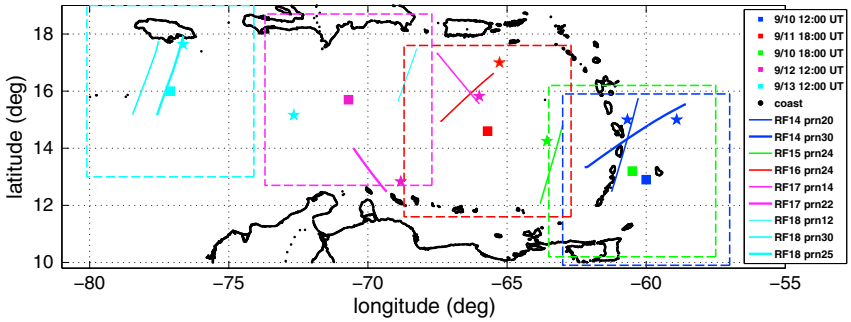

Figure 10. The mesoscale α [*Wang*, 2012] storm region is defined for each day with a 6° by 6° box around the National Hurricane Center best track Pre-Karl storm positions (squares) for the period 10–13 September 2010. Tangent point paths (thin lines) are shown for the occultations tracked by GISMOS geodetic receivers during missions RF14 thru RF18. The pre-Karl disturbance developed into a tropical depression and then tropical storm on 14 September, 1 day after RF18 (cyan).

dropsonde refractivity variations about the mean are more than 3 times the dry refractivity standard deviation. This illustrates that over this pregenesis time period, the refractivity variations from the surface to as high as 9.4 km are associated primarily with moisture rather than temperature variations.

Komaromi [2013] found a warm core temperature anomaly up to 2 K in the upper troposphere of developing PREDICT tropical disturbances over the 24 h period before genesis. This would lead to a 0.5% variation in refractivity, so any warm core signature in the ARO profiles remains small in comparison to the moisture signal. Relative to this background, the 3–10% variation due to moisture variations dominates the refractivity profiles. We conclude that direct observations of ARO refractivity will definitely be a sensitive indicator of humidity variations in this type of environment. Of course, the signals from both the warming core and changes in humidity are contained in the refractivity measurement, and would impact both fields in a data assimilation experiment.

The pre-Karl storm track positions provided by the NHC (www.nhc.noaa.gov) and the occultation tangent point paths tracked by GISMOS geodetic receivers over the same period are shown in Figure 10. Nine ARO refractivity profiles were available for 10–13 September. No usable retrievals were available from the geodetic receiver data from RF19 on 14 September, although data are available from the GRS system (see section 5).

The dynamically protected region hypothesized to enable thermodynamically favorable conditions for tropical cyclone development is on the meso α scale [*Wang*, 2012]. We used a 6° by 6° box as defined by *Wang* [2012] around the NHC best track storm locations to describe this region. Seven of the nine ARO refractivity profiles fall within this distance range and were used to examine the change in refractivity over the development of the system from day T-4, 10 September, until day T-1, 13 September, where T is the day of genesis of the tropical storm (boxes in Figure 10). ARO occultations PRN25 and PRN30 from RF14 (10 September, T-4), PRN24 from RF15 (T-4), PRN24 from RF16 (T-3), PRN22 from RF17 (T-2), and PRN25 and PRN30 from RF18 (T-1), fall within this spatial scale. These profiles are compared to the pre-Karl environmental mean refractivity in Figure 11, where the profile differences are labeled by time before genesis. The seven ARO profiles were sampled between 8 A.M. and 4 P.M. local time. The largest change from 1 day to the next is 4%, and we can conclude, based on the small-temperature variation shown in Figure 9c, that the refractivity variation is primarily due to moisture. The two RF14 occultations from day T-4 have the lowest refractivity while the refractivity of the RF15 (T-4), RF16 (T-3), and RF18 (T-1) profiles are greater, consistent with moistening within the mesoscale area containing the storm center as pre-Karl disturbance approaches genesis. This preliminary result is based on only a limited number of profiles but is consistent with the increase in moisture observed at middle to upper levels in the interior of the tropical wave for the pre-Karl case [*Davis and Ahijevych*, 2012; *Smith and Montgomery*, 2012].

5. Discussion

As noted above, the ARO refractivity agrees best with dropsondes and the ERAI reanalysis in the range from 7 to 12 km; however, there are profiles that deviate greatly below 7 km as moisture levels increase in the lower troposphere [*Sokolovskiy*, 2001]. Sharp gradients in moisture can create atmospheric multipath, where the measured Doppler shifts will not represent unique signal paths but composites of more than one signal arriving

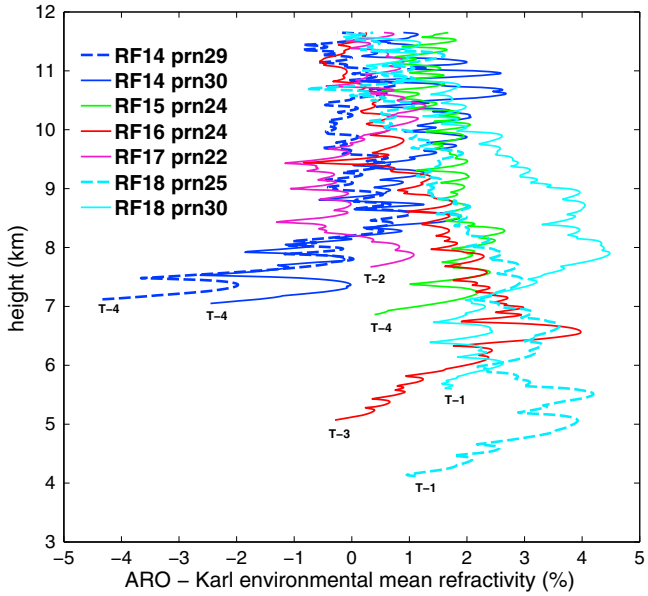

Figure 11. The refractivity difference as a function of time relative to the pre-Karl environmental mean indicates greater moisture at midlevels as the storm system evolves. For example, refractivity on 10 September (dark blue) 4 days prior to genesis (T-4) is relatively low above 7 km, likely indicating dry air, and refractivity is high on 13 September (cyan) at T-1. Genesis of pre-Karl to tropical storm strength occurred on 14 September 2010 (T-0).

at the receiver simultaneously [*Melbourne*, 2005]. The increased error in cases extending below 7 km near the end of tracking is likely due to atmospheric multipath [*Ao et al.*, 2003; *Sokolovskiy*, 2001]. Additionally, the greater variability of moisture discussed in section 4.3 (Figure 9b) and resulting variability in refractivity can exacerbate differences resulting from spatiotemporal mismatches. Closer agreement was achieved as expected at higher altitudes, where refractivity is dominated by temperature and refractivity is less variable horizontally.

The geodetic GPS receivers were included in the GISMOS design in order to provide straightforward verification of system operation without complex signal analysis. The majority of refractivity profiles retrieved from the geodetic GPS receivers do not extend below 6–7 km height, and only a few of the many possible occultations were successfully recorded by these receivers. Even in this limited height range, however, it is possible to see significant variations in moisture. The dropsonde data in Figure 9 illustrate that the variability at this height is still dominated by moisture rather than temperature variations over the 4 day genesis period for Karl. In studies of other storms during PREDICT, moisture variability in the upper tropospheric levels was associated with dry air intrusion from large-scale subsidence or advection that can suppress deep convection and tropical cyclone formation [*Fritz and Wang*, 2013; *Wang*, 2012]; therefore, it is useful to have these observations above 6 km. However, further science benefit will result from the data analysis from the GRS instrumentation that samples the raw RF signal and penetrates deeper into the low to middle tropospheric region that is important to deep convection.

An example of the total number of possible setting and rising occultations is shown in Figure 12 for research flight RF18. The 14 possible ARO profiles that can be retrieved with open-loop tracking is a significant increase over the one available COSMIC spaceborne profile during the time period of RF18 and the three ARO profiles retrieved by the GISMOS geodetic receivers (Figure 12). The geodetic GPS receivers recorded only a small subset of occultations because the conventional phase-locked loop tracking relies on feedback from the incoming signal to maintain a zero phase error between the incoming signal and replica. They typically lose lock on the signal if there are rapid phase changes or large fluctuations in signal amplitude, as can be produced by sharp gradients in refractivity. These types of signal variations are expected to occur in the middle to lower troposphere where moisture is increasing with decreasing altitude and has higher variability. This has been extensively observed in GPS/MET and CHAMP [*Ao et al.*, 2003; *Rocken et al.*, 1997]. The early termination of tracking at low altitudes was expected and influenced the design of the earliest spaceborne occultation receivers [*Melbourne*, 2005], as well as the design of GISMOS [*Garrison et al.*, 2007]. GISMOS was designed with the GRS to sample the raw GPS signals at 10 MHz for later postprocessing with a software receiver. An open-loop tracking algorithm uses an a priori geometric model of the Doppler shift that does not rely on signal feedback for tracking Doppler in the postprocessing. This method avoids the problems introduced by rapidly changing phase, allows recovery of the data deeper into the moist lower troposphere, and makes analysis of rising occultations possible [*Lulich et al.*, 2010; *Sokolovskiy*, 2001], (K.-N. Wang et al., Open-loop tracking of rising and setting GPS radio occultation signals from an airborne platform: Signal model and error analysis, submitted to *Transactions on Geoscience and Remote Sensing*, 2015). Data from a test

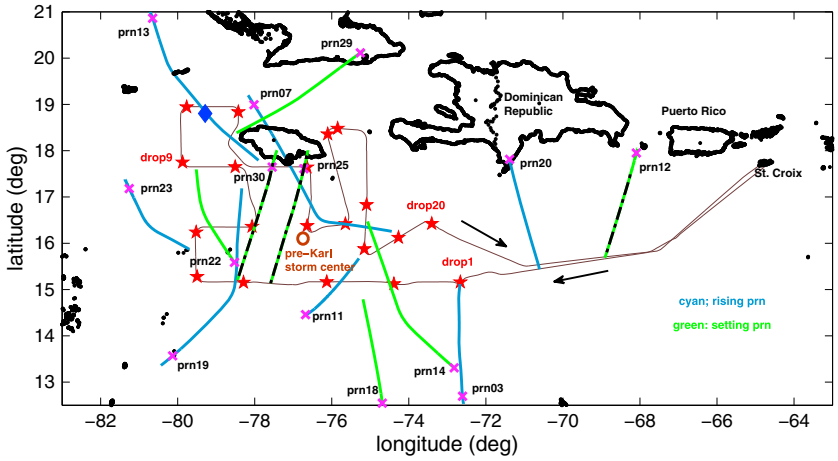

Figure 12. Flight path of RF18 on 13 September 2010, 10:00–16:00 UT. Tangent point paths of rising and setting occultations are shown in cyan and green, respectively. Setting occultations (PRN12, 25 and 30) are overlaid with a black dashed line. Dropsonde locations are marked by red stars, and ARO occultation points are marked with magenta crosses. The occultation point of the single COSMIC retrieval (13:00 UT) available during RF18 is marked by the blue diamond.

case were analyzed with the open-loop method for occulting PRN25 during RF18, and the resulting refractivity profile was compared to the result from the Trimble NetRS conventional geodetic receiver (Figures 13a and 13b) [*Haase et al.*, 2014]. The open-loop result extends about 2 km lower than the profile from the geodetic receiver. The small differences between the two profiles are much smaller than the differences found in the dropsonde comparisons.

Rising occultations can be analyzed using the open-loop approach as well, since it operates on the prerecorded intermediate-frequency GPS data, so signal acquisition and initiation of tracking can occur after the satellite reaches a high elevation. In a second test case of open-loop tracking, the RF18 PRN20 rising occultation was retrieved beginning near 4 km altitude (Figure 13c). The use of open-loop tracking has demonstrated superior results in previous GISMOS validation campaigns and produced one to two rising or setting occultations per hour of flight [*Muradyan*, 2012]. A preliminary analysis of the recovered carrier phase signals from PREDICT indicates that 10 to 15 ARO profiles will be available for each mission, comparable to the number of dropsondes released. The open-loop tracking data set will contribute a significantly increased number of profiles so that the

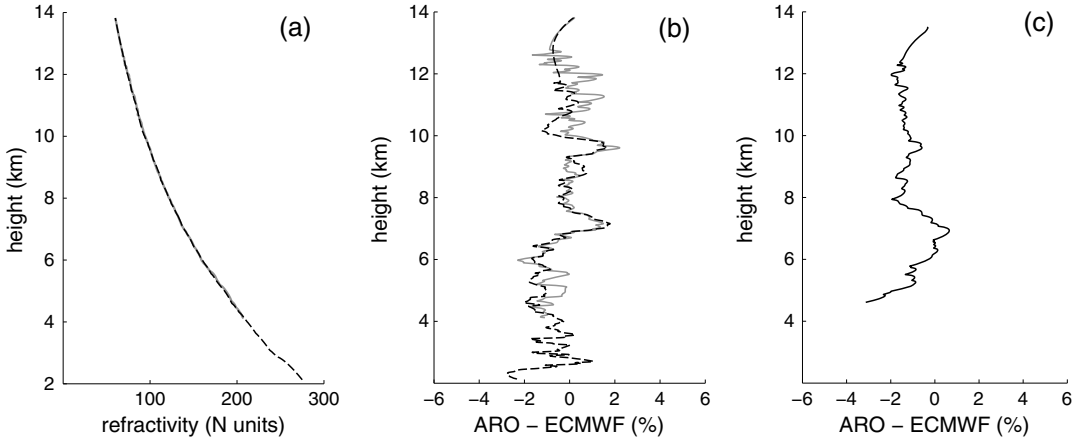

Figure 13. (a) Comparison of the open-loop refractivity retrieval (dashed line) with the conventional geodetic receiver refractivity retrieval (gray) for the RF18 PRN25 occultation. The open-loop method tracked ~2 km lower than the geodetic receiver. (b) Percent refractivity difference relative to the ECMWF Interim reanalysis profile for the open-loop retrieval (dashed line) and conventional geodetic receiver retrieval (gray). (c) Percent refractivity difference relative to the ECMWF Interim reanalysis profile for rising RF18 PRN20 occultation.

statistics can be evaluated at lower altitudes, and with respect to temporal and spatial separation as has been carried out for spaceborne RO [i.e., *Chen et al*., 2011]. The analysis of the open-loop tracking data is ongoing and will be the subject of future work.

While the geometric optics retrieval technique was adequate above 6–7 km, it is possible that the refractivity errors below that height are increased due to atmospheric multipath just prior to loss of signal tracking. The small number of profiles that extend below 6 km is insufficient to provide a statistically robust conclusion. However, the availability of the open-loop data will make it worthwhile to implement the Full Spectrum Inversion method [*Jensen et al*., 2003, 2006], for example, to extend the profiles further into the lower troposphere in the presence of atmospheric multipath.

The extensive GPS ARO data set was collected with the ultimate goal of providing additional data for assimilation into numerical models to improve tropical cyclone forecasts. Given that previous case studies that assimilated sparsely sampled COSMIC spaceborne RO data indicate an improvement to numerical forecasts of hurricane development [*Huang et al*., 2010; *Liu et al*., 2012], assimilation of the denser observations possible with ARO [*Lesne et al*., 2002], particularly in the near-storm environment (Figure 12), could potentially show significant further impact on hurricane forecasts. The nonlocal refractivity assimilation operator for the Weather and Research Forecasting Data Assimilation system has been developed for airborne observations based on *Zou et al*. [1999]. It includes the modifications for the asymmetric recording geometry below flight level and assimilation of observations at each height at the actual horizontal location of the tangent point to account for the larger tangent point drift of airborne observations, thus mitigating the impact of the spherical symmetry assumption [*Haase et al*., 2012]. The future results from the complete ARO open-loop tracking analysis will be useful for this assimilation study.

The assimilation of dropsonde and airborne radio occultation observations into NWP models is complementary, since dropsondes measure the local properties at specific points, and the ARO observations measure the properties of the larger-scale environment. Dropsondes measure temperature and moisture directly and additionally provide wind observations. However, dropsondes have a high cost per observation (~$700), require special modifications to the aircraft, permission from air traffic control for release, and have significant safety restrictions that limit deployments over land. The ARO technique, on the other hand, has the potential to be adapted to a wider range of aircraft for continuous observations at low additional cost.

6. Conclusions

The GISMOS airborne radio occultation (ARO) system was deployed during the PRE-Depression Investigation of Cloud systems in the Tropics (PREDICT) field experiment and operated continuously throughout the 45 day campaign. The system includes a conventional geodetic GPS receiver component for straightforward validation of the analysis method in the middle to upper troposphere, and a high-sample rate (10 MHz) GPS recorder for postprocessing of complex signals that probe the lower troposphere. This is the first study to assess the quality of ARO data and to demonstrate the potential of this new technique as well as provide a first look at the usefulness of the technique for observing moisture variability above 6 km with the complete geodetic GPS receiver data set.

A data set of 21 ARO refractivity profiles was retrieved that sampled the atmosphere in the environment of six tropical disturbances, several of which developed into tropical storms. The ARO profiles were compared with refractivity profiles calculated from the PREDICT dropsonde data and with refractivity profiles derived from the ECMWF Interim reanalysis within about 30 km of the occultation point. Overall, the ARO refractivity compared favorably with PREDICT dropsonde refractivity and ERA-Interim refractivity, even in this rapidly changing heterogeneous environment. The standard deviation of the difference of the ARO refractivity from dropsondes did not exceed 1.5%, and the bias was less than 0.5% from 7 to 12 km altitude. The standard deviation of the difference of the airborne refractivity from ERA-Interim was less than 2%, and the bias was also less than 0.5% over the 7–12 km height range. These values are comparable to results found at similar tropical latitudes for spaceborne radio occultation profiles, even though the ARO sampling was primarily in challenging near-storm environments with highly variable moisture fields.

Refractivity profiles were shown for seven occultations in the environment of the pre-Karl tropical disturbance over the pregenesis period 10–13 September 2010. Dropsondes over this period show that in the tropical

environment, the refractivity variations are primarily indicative of moisture variations rather than temperature. With this limited preliminary data set available from the conventional geodetic GPS receivers, we found that the change in the measured refractivity of the ARO profiles relative to the pre-Karl environmental mean refractivity was consistent with moistening in the vicinity of the pre-Karl storm center [*Davis and Ahijevych*, 2012; *Smith and Montgomery*, 2012]. One day prior to genesis, the ARO profile nearest the NHC best track location had systematically higher refractivity relative to the pre-Karl environmental mean over the 7–10 km height interval. In contrast, 4 days prior to genesis, the profile nearest the center had refractivity consistent with the background environmental mean over that height range. This example illustrates that the ARO technique is capable of making reliable measurements in the near-storm region.

The conventional GPS geodetic receivers performed surprisingly well in this moist tropical environment using standard GPS avionics antennas for setting occultations above 7 km. The relatively small number of occultations available was due to the limitations of phase-locked loop tracking, so the profiles were not tracked consistently below 6–7 km height and no rising occultations were observed. GISMOS was designed with the additional 10 MHz GNSS recording system (GRS) to handle this well-known difficulty. With the data recorded during PREDICT from this instrument, it will be possible to retrieve many more profiles from the recorded occultation data (on the order of 10–15 per flight). In a test case, the occultation of PRN25 during RF18 was measured using open-loop tracking. The refractivity profile retrieved from the open-loop technique extends about 2 km below the lower limit of the profile obtained using data from the conventional receiver. In addition to tracking GPS signals lower in the troposphere, rising occultations can be reliably measured by using the open-loop tracking, which was not possible with the geodetic GPS receivers. The combination of the additional rising occultations with an increase in the measured setting occultations will result in a valuable data set for testing the impact of assimilating ARO data on improving tropical storm genesis, intensity, and track during the PREDICT campaign, as well as characterizing the near-storm environment for each case.

Acknowledgments

The analyzed refractivity profiles are available at the webpage http://www.igpppublic.ucsd.edu/~jhaase/airborne_ro. This work was funded by contributions from the following grants: HIAPER UCAR subcontract S05-39696, NSF grant SGER-0802887, NSF grant AGS 1015904, NSF grant AGS 1301835, and NASA grant NNX12AK30G. Partial support for B.M. was provided by the Ross Fellowship. P.M. was supported by the Schlumberger Faculty for the Future Fellowship. We would also like to thank the following: Ulvi Acikoz, Tyler Lulich, and Brian Ventre who contributed to software development for our use in the open-loop analysis; Alexandria Johnson who assisted with the GISMOS data collection and preliminary analysis during the PREDICT campaign; J. Jensen, J. Meitin, A. Cooper, A. Schanot, R. Sherman, and the NCAR-EOL and NCAR-RAF staff for their logistical support during the PREDICT campaign; PREDICT PI's M. Montgomery and C. Davis; M. Bell, D. Raymond, and C. Lopez who assisted with GISMOS operation; and J. Dunion, J. Cordeira, K. Griffin, and the PREDICT/NASA/NOAA forecast teams. ERAI reanalyses were provided by the European Center for Medium-Range Forecasts (ECMWF), http://apps.ecmwf.int/datasets/, and PREDICT dropsonde data were provided by NCAR-EOL sponsored by the NSF, http://data.eol.ucar.edu/master_list/?project=PREDICT. Radiosonde data were provided through the University of Wyoming, Department of Atmospheric Science website, http://weather.uwyo.edu/upperair/sounding.html. GOES-13 imagery obtained from the NASA EOSDIS Global Hydrology Resource Center (GHRC) DAAC, Huntsville, AL, http://ghrc.nsstc.nasa.gov/hydro/. We thank UNAVCO for technical support with testing and operation of the commercial GPS receivers. We thank Chris Davis for an early review of this paper, and the editor and four anonymous reviewers for their helpful comments.

References

Anthes, R. A. (2011), Exploring Earth's atmosphere with radio occultation: Contributions to weather, climate and space weather, *Atmos. Meas. Technol.*, *4*(6), 1077–1103.

Anthes, R. A., et al. (2008), The COSMIC/FORMOSAT-3 Mission: Early results, *Bull. Am. Meteorol. Soc.*, *89*(3), 313–333, doi:10.1175/bams-89-3-313.

Ao, C. O., T. K. Meehan, G. A. Hajj, A. J. Mannucci, and G. Beyerle (2003), Lower troposphere refractivity bias in GPS occultation retrievals, *J. Geophys. Res.*, *108*(D18), 4577, doi:10.1029/2002JD003216.

Beutler, G., M. Rothacher, S. Schaer, T. A. Springer, J. Kouba, and R. E. Neilan (1999), The International GPS Service (IGS): An interdisciplinary service in support of Earth sciences, *Adv. Space Res.*, *23*(4), 631–653, doi:10.1016/S0273-1177(99)00160-X.

Beutler, G., A. Moore, and I. Mueller (2009), The international global navigation satellite systems service (IGS): Development and achievements, *J. Geod.*, *83*(3-4), 297–307, doi:10.1007/s00190-008-0268-z.

Bevis, M., S. Businger, S. Chiswell, T. A. Herring, R. A. Anthes, C. Rocken, and R. H. Ware (1994), GPS meteorology: Mapping zenith wet delays onto precipitable water, *J. Appl. Meteorol.*, *33*(3), 379–386.

Biondi, R., T. Neubert, S. Syndergaard, and J. K. Nielsen (2011), Radio occultation bending angle anomalies during tropical cyclones, *Atmos. Meas. Tech.*, *4*(6), 1053–1060, doi:10.5194/amt-4-1053-2011.

Biondi, R., S.-P. Ho, W. Randel, S. Syndergaard, and T. Neubert (2013), Tropical cyclone cloud-top height and vertical temperature structure detection using GPS radio occultation measurements, *J. Geophys. Res. Atmos.*, *118*, 5247–5259, doi:10.1002/jgrd.50448.

Born, M., and E. Wolf (1999), *Principles of Optics: Electromagnetic Theory of Propagation, Interference and Diffraction of Light*, 7th (expanded) ed., 952 pp., Cambridge Univ. Press, Cambridge, U. K.

Chen, S. Y., C. Y. Huang, Y. H. Kuo, Y. R. Guo, and S. Sokolovskiy (2009), Assimilation of GPS refractivity from FORMOSAT-3/COSMIC using a nonlocal operator with WRF 3DVAR and its impact on the prediction of a typhoon event, *Terr. Atmos. Ocean. Sci.*, *20*, 133–154, doi:10.3319/TAO.2007.11.29.01(F3C).

Chen, S. Y., C. Y. Huang, Y. H. Kuo, and S. Sokolovskiy (2011), Observational error estimation of FORMOSAT-3/COSMIC GPS radio occultation data, *Mon. Weather Rev.*, *139*(3), 853–865.

Davis, C. A., and D. A. Ahijevych (2012), Mesoscale structural evolution of three tropical weather systems observed during PREDICT, *J. Atmos. Sci.*, *69*(4), 1284–1305, doi:10.1175/jas-d-11-0225.1.

Davis, C. A., D. A. Ahijevych, J. A. Haggerty, and M. J. Mahoney (2014), Observations of temperature in the upper troposphere and lower stratosphere of tropical weather disturbances, *J. Atmos. Sci.*, *71*(5), 1593–1608, doi:10.1175/Jas-D-13-0278.1.

Dee, D. P., et al. (2011), The ERA-Interim reanalysis: Configuration and performance of the data assimilation system, *Q. J. R. Meteorol. Soc.*, *137*(656), 553–597, doi:10.1002/qj.828.

Dunkerton, T. J., M. T. Montgomery, and Z. Wang (2009), Tropical cyclogenesis in a tropical wave critical layer: Easterly waves, *Atmos. Chem. Phys.*, *9*(15), 5587–5646.

Durre, I., T. Reale, D. Carlson, J. Christy, M. Uddstrom, M. Gelman, and P. Thorne (2005), Improving the usefulness of operational radiosonde data, *Bull. Am. Meteorol. Soc.*, *86*(3), 411–416, doi:10.1175/BAMS-86-3-411.

Evans, C., et al. (2012), The PRE-Depression Investigation of Cloud-Systems in the Tropics (PREDICT) field campaign perspectives of early career scientists, *Bull. Am. Meteorol. Soc.*, *93*(2), 173–187.

Fjeldbo, G., A. J. Kliore, and V. R. Eshleman (1971), The neutral atmosphere of Venus as studied with the Mariner V radio occultation experiments, *Astron. J.*, *76*(2), 123–140.

Fritz, C., and Z. Wang (2013), A numerical study of the impacts of dry air on tropical cyclone formation: A development case and a nondevelopment case, *J. Atmos. Sci.*, *70*(1), 91–111, doi:10.1175/Jas-D-12-018.1.
Garrison, J. L., M. Walker, J. S. Haase, T. Lulich, F. Xie, B. D. Ventre, M. H. Boehme, B. Wilmhoff, and S. J. Katzberg (2007), Development and testing of the GISMOS instrument, paper presented at IEEE International Geoscience and Remote Sensing Symposium, Barcelona, Spain, 23–27 July.
Gorbunov, M. E. (2002), Canonical transform method for processing radio occultation data in the lower troposphere, *Radio Sci.*, *37*(5), 1076, doi:10.1029/2000RS002592.
Gorbunov, M. E., and K. B. Lauritsen (2004), Canonical transform methods for radio occultation data, in *Occultations for Probing Atmosphere and Climate*, edited by G. Kirchengast, U. Foelsche, and A. Steiner, pp. 61–68, Springer, Berlin, doi:10.1007/978-3-662-09041-1_6.
Gorbunov, M. E., H. H. Benzon, A. S. Jensen, M. S. Lohmann, and A. S. Nielsen (2004), Comparative analysis of radio occultation processing approaches based on Fourier integral operators, *Radio Sci.*, *39*, RS6004, doi:10.1029/2003RS002916.
Haase, J. S., B. Murphy, X.-M. Chen, S.-H. Chen, P. Muradyan, F. G. Nievinski, K. M. Larson, J. L. Garrison, K.-N. Wang, and S.-Y. Chen (2012), Preliminary results from the retrieval and assimilation of GPS radio occultation refractivity observations during tropical storm development, paper presented at 2012 Fall Meeting, AGU, San Francisco, Calif., 3–7 Dec.
Haase, J. S., B. J. Murphy, P. Muradyan, F. Nievinski, K. M. Larson, J. L. Garrison, and K.-N. Wang (2014), First results from an airborne GPS radio occultation system for atmospheric profiling, *Geophys. Res. Lett.*, *40*, 1759–1765, doi:10.1002/2013GL058681.
Hajj, G. A., E. R. Kursinski, L. J. Romans, W. I. Bertiger, and S. S. Leroy (2002), A technical description of atmospheric sounding by GPS occultation, *J. Atmos. Sol. Terr. Phys.*, *64*(4), 451–469.
Hajj, G. A., C. O. Ao, B. A. Iijima, D. Kuang, E. R. Kursinski, A. J. Mannucci, T. K. Meehan, L. J. Romans, M. D. Juarez, and T. P. Yunck (2004), CHAMP and SAC-C atmospheric occultation results and intercomparisons, *J. Geophys. Res.*, *109*, D06109, doi:10.1029/2003JD003909.
Healy, S. B. (2011), Refractivity coefficients used in the assimilation of GPS radio occultation measurements, *J. Geophys. Res.*, *116*, D01106, doi:10.1029/2010JD014013.
Healy, S. B., and J. R. Eyre (2000), Retrieving temperature, water vapour and surface pressure information from refractive-index profiles derived by radio occultation: A simulation study, *Q. J. R. Meteorol. Soc.*, *126*, 1661–1683.
Healy, S. B., J. S. Haase, and O. Lesne (2002), Abel transform inversion of radio occultation measurements made with a receiver inside the Earth's atmosphere, *Ann. Geophys.*, *20*(8), 1253–1256.
Hofmann-Wellenhof, B., and H. Moritz (2006), *Physical Geodesy*, 403 pp., Springer, New York.
Houze, R. A., W.-C. Lee, and M. M. Bell (2009), Convective contribution to the genesis of hurricane Ophelia (2005), *Mon. Weather Rev.*, *137*(9), 2778–2800, doi:10.1175/2009MWR2727.1.
Huang, C. Y., et al. (2010), Impact of GPS radio occultation data assimilation on regional weather predictions, *GPS Solutions*, *14*(1), 35–49.
Jensen, A. S., M. S. Lohmann, H. H. Benzon, and A. S. Nielsen (2003), Full spectrum inversion of radio occultation signals, *Radio Sci.*, *38*(3), 1040, doi:10.1029/2002RS002763.
Jensen, A. S., M. S. Lohmann, A. S. Nielsen, and H. H. Benzon (2004), Geometrical optics phase matching of radio occultation signals, *Radio Sci.*, *39*, RS3009, doi:10.1029/2003RS002899.
Jensen, A. S., H. H. Benzon, A. S. Nielsen, and M. S. Lohmann (2006), Processing radio occultation data by full spectrum inversion techniques: An overview and recent developments, in *Atmosphere and Climate*, edited by U. Foelsche, G. Kirchengast, and A. Steiner, pp. 95–112, Springer, Berlin, doi:10.1007/3-540-34121-8_9.
Jin, S. (2013), *GNSS Remote Sensing: Theory, Methods and Applications*, 276 pp., Springer, Dordrecht, Netherlands.
Kidder, S. Q., M. D. Goldberg, R. M. Zehr, M. DeMaria, J. F. W. Purdom, C. S. Velden, N. C. Grody, and S. J. Kusselson (2000), Satellite analysis of tropical cyclones using the Advanced Microwave Sounding Unit (AMSU), *Bull. Am. Meteorol. Soc.*, *81*(6), 1241–1259, doi:10.1175/1520-0477(2000)081<1241:SAOTCU>2.3.CO;2.
Komaromi, W. A. (2013), An investigation of composite dropsonde profiles for developing and nondeveloping tropical waves during the 2010 PREDICT field campaign, *J. Atmos. Sci.*, *70*(2), 542–558.
Kuo, Y. H., T. K. Wee, S. Sokolovskiy, C. Rocken, W. Schreiner, D. Hunt, and R. A. Anthes (2004), Inversion and error estimation of GPS radio occultation data, *J. Meteorol. Soc. Jpn.*, *82*(1B), 507–531.
Kuo, Y. H., W. S. Schreiner, J. Wang, D. L. Rossiter, and Y. Zhang (2005), Comparison of GPS radio occultation soundings with radiosondes, *Geophys. Res. Lett.*, *32*, L05817, doi:10.1029/2004GL021443.
Kursinski, E. R., G. A. Hajj, K. R. Hardy, J. T. Schofield, and R. Linfield (1997), Observing Earth's atmosphere with radio occultation measurements, *J. Geophys. Res.*, *102*, 23,429–23,465, doi:10.1029/97JD01569.
Landsea, C. W. (1993), A climatology of intense (or major) Atlantic hurricanes, *Mon. Weather Rev.*, *121*, 1703–1713.
Lesne, O., J. S. Haase, G. Kirgast, J. Ramsauer, and W. Poetzi (2002), Sensitivity analysis of GNSS radio occultation for airborne sounding of the troposphere, *Phys. Chem. Earth*, *27*(4-5), 291–299.
Liu, H., J. Anderson, Y.-H. Kuo, C. Snyder, and A. Caya (2008), Evaluation of a nonlocal quasi-phase observation operator in assimilation of CHAMP radio occultation refractivity with WRF, *Mon. Weather Rev.*, *136*(1), 242–256, doi:10.1175/2007MWR2042.1.
Liu, H., J. Anderson, and Y. H. Kuo (2012), Improved analyses and forecasts of hurricane Ernesto's genesis using radio occultation data in an ensemble filter assimilation system, *Mon. Weather Rev.*, *140*(1), 151–166.
Lulich, T. D., J. L. Garrison, J. S. Haase, Y.-M. Yang, J. Voo, F. Xie, and P. Muradyan (2010), Open loop tracking of radio occultation signals from an airborne platform, paper presented at Proceedings of the 23rd International Technical Meeting of the Satellite Division of the Institute of Navigation (ION GNSS 2010), Portland, Oregon, 21–24 Sept.
Ma, Z., Y.-H. Kuo, B. Wang, W.-S. Wu, and S. Sokolovskiy (2009), Comparison of local and nonlocal observation operators for the assimilation of GPS RO data with the NCEP GSI system: An OSSE study, *Mon. Weather Rev.*, *137*(10), 3575–3587, doi:10.1175/2009MWR2809.1.
Melbourne, W. G. (2005), *Radio Occultations Using Earth Satellites: A Wave Theory Treatment*, xxiv, 647 pp., Wiley-Interscience, Hoboken, N. J.
Merrill, R. T. (1991), Physical retrieval of typhoon structure using passive microwave observations, in *Preprints, 19th Conf. on Hurricanes and Tropical Meteorology*, edited, pp. 405–408, American Meteorology Society, Miami, Fla.
Misra, P., and P. Enge (2006), *Global Positioning System: Signals, Measurements, and Performance*, 2nd ed., 569 pp., Ganga-Jamuna Press, Lincoln, Mass.
Montgomery, M. T., et al. (2012), The PRE-Depression Investigation of Cloud systems in the Tropics (PREDICT) experiment: Scientific basis, new analysis tools and some first results, *Bull. Am. Meteorol. Soc.*, *92*(9), 153–172, doi:10.1175/BAMS-D-11-00046.1.
Moradi, I., B. Soden, R. Ferraro, P. Arkin, and H. Vömel (2013), Assessing the quality of humidity measurements from global operational radiosonde sensors, *J. Geophys. Res. Atmos.*, *118*, 8040–8053, doi:10.1002/jgrd.50589.
Mostafa, M., J. Hutton, and B. Reid (2001), GPS/IMU products- the Applanix approach, paper presented at Photogrammetric Week, University of Stuttgart, Institute for Photgrammetry, Stuttgart, 24–28 Sept.
Muradyan, P. (2009), GPS/INS navigation precision and its effect on airborne radio occultation, MS thesis, 93 pp., Purdue University, West Lafayette, Indiana.

Muradyan, P. (2012), Profiling the atmosphere with the airborne GPS radio occultation technique using open-loop tracking, PhD thesis, 196 pp., Purdue Univ., West Lafayette, Indiana.
Muradyan, P., J. S. Haase, F. Xie, J. L. Garrison, T. Lulich, and J. Voo (2010), GPS/INS navigation precision and its effect on airborne radio occultation retrieval accuracy, *GPS Solutions*, doi:10.1007/s10291-010-0183-7.
Pavlis, N. K., S. A. Holmes, S. C. Kenyon, and J. K. Factor (2012), The development and evaluation of the Earth Gravitational Model 2008 (EGM2008), *J. Geophys. Res.*, *117*, B04406, doi:10.1029/2011JB008916.
Poli, P., S. B. Healy, F. Rabier, and J. Pailleux (2008), Preliminary assessment of the scalability of GPS radio occultations impact in numerical weather prediction, *Geophys. Res. Lett.*, *35*, L23811, doi:10.1029/2008GL035873.
Poli, P., S. B. Healy, and D. P. Dee (2010), Assimilation of global positioning system radio occultation data in the ECMWF ERA-Interim reanalysis, *Q. J. R. Meteorol. Soc.*, *136*(653), 1972–1990, doi:10.1002/qj.722.
Reale, T., B. Sun, F. H. Tilley, and M. Pettey (2012), The NOAA Products Validation System (NPROVS), *J. Atmos. Oceanic Technol.*, *29*(5), 629–645, doi:10.1175/JTECH-D-11-00072.1.
Rocken, C., et al. (1997), Analysis and validation of GPS/MET data in the neutral atmosphere, *J. Geophys. Res.*, *102*, 29,849–29,866, doi:10.1029/97JD02400.
Rodgers, C. D. (1976), Retrieval of atmospheric temperature and composition from remote measurements of thermal radiation, *Rev. Geophys.*, *14*, 609–624, doi:10.1029/RG014i004p00609.
Schafer, R. W. (2011), What is a Savitzky-Golay filter?, *IEEE Signal Process Mag.*, *28*(4), 111–117.
Schreiner, W., C. Rocken, S. Sokolovskiy, S. Syndergaard, and D. Hunt (2007), Estimates of the precision of GPS radio occultations from the COSMIC/FORMOSAT-3 mission, *Geophys. Res. Lett.*, *34*, L04808, doi:10.1029/2006GL027557.
Smith, E. K., and S. Weintraub (1953), The constants in the equation for atmospheric refractive index at radio frequencies, *Proc. IRE*, *41*(8), 1035–1037.
Smith, R. K., and M. T. Montgomery (2012), Observations of the convective environment in developing and non-developing tropical disturbances, *Q. J. R. Meteorol. Soc.*, *138*(668), 1721–1739.
Sokolovskiy, S. (2001), Tracking tropospheric radio occultation signals from low Earth orbit, *Radio Sci.*, *36*, 483–498, doi:10.1029/1999RS002305.
Sokolovskiy, S., Y.-H. Kuo, and W. Wang (2005a), Assessing the accuracy of a linearized observation operator for assimilation of radio occultation data: Case simulations with a high-resolution weather model, *Mon. Weather Rev.*, *133*(8), 2200–2212, doi:10.1175/MWR2948.1.
Sokolovskiy, S., Y. H. Kuo, and W. Wang (2005b), Evaluation of a linear phase observation operator with CHAMP radio occultation data and high-resolution regional analysis, *Mon. Weather Rev.*, *133*(10), 3053–3059.
Sun, B., A. Reale, D. J. Seidel, and D. C. Hunt (2010), Comparing radiosonde and COSMIC atmospheric profile data to quantify differences among radiosonde types and the effects of imperfect collocation on comparison statistics, *J. Geophys. Res.*, *115*, D23104, doi:10.1029/2010JD014457.
Sun, B., A. Reale, S. Schroeder, D. J. Seidel, and B. Ballish (2013), Toward improved corrections for radiation-induced biases in radiosonde temperature observations, *J. Geophys. Res. Atmos.*, *118*, 4231–4243, doi:10.1002/jgrd.50369.
Syndergaard, S. (1998), Modeling the impact of the Earth's oblateness on the retrieval of temperature and pressure profiles from limb sounding, *J. Atmos. Sol. Terr. Phys.*, *60*(2), 171–180.
Tsuda, T., X. Lin, H. Hayashi, and Noersomadi (2011), Analysis of vertical wave number spectrum of atmospheric gravity waves in the stratosphere using COSMIC GPS radio occultation data, *Atmos. Meas. Tech.*, *4*(8), 1627–1636, doi:10.5194/amt-4-1627-2011.
Vergados, P., A. J. Mannucci, and H. Su (2013), A validation study for GPS radio occultation data with moist thermodynamic structure of tropical cyclones, *J. Geophys. Res. Atmos.*, *118*, 9401–9413, doi:10.1002/jgrd.50698.
Vergados, P., Z. J. Luo, K. Emanuel, and A. J. Mannucci (2014), Observational tests of hurricane intensity estimations using GPS radio occultations, *J. Geophys. Res. Atmos.*, *119*, 1936–1948, doi:10.1002/2013JD020934.
von Engeln, A., Y. Andres, C. Marquardt, and F. Sancho (2011), GRAS radio occultation on-board of Metop, *Adv. Space Res.*, *47*(2), 336–347.
Voo, J. K., J. L. Garrison, J. S. Haase, and T. D. Lulich (2009), Recent experiments in ocean remote sensing with bistatic radar using global navigation satellite signals, in *2009 IEEE Radar Conference, Pasadena, Calif.*, edited, p. 5, IEEE, New York, doi:10.1109/RADAR.2009.4977115.
Vorob'ev, V. V., and T. G. Krasil'nikova (1994), Estimation of the accuracy of the atmospheric refractive index recovery from Doppler shift measurements at frequencies used in the NAVSTAR system, *Phys. Atmos. Ocean (Engl. Transl.)*, *29*(5), 602–609.
Wang, J. H. (2005), Evaluation of the dropsonde humidity sensor using data from DYCOMS-II and IHOP_2002, *J. Atmos. Oceanic Technol.*, *22*(3), 247–257, doi:10.1175/Jtech1698.1.
Wang, J. H., J. C. Bian, W. O. Brown, H. Cole, V. Grubisic, and K. Young (2009), Vertical air motion from T-REX radiosonde and dropsonde data, *J. Atmos. Oceanic Technol.*, *26*(5), 928–942, doi:10.1175/2008jtecha1240.1.
Wang, Z. (2012), Thermodynamic aspects of tropical cyclone formation, *J. Atmos. Sci.*, *69*(8), 2433–2451, doi:10.1175/jas-d-11-0298.1.
Wang, Z., M. T. Montgomery, and T. J. Dunkerton (2009), A dynamically-based method for forecasting tropical cyclogenesis location in the Atlantic sector using global model products, *Geophys. Res. Lett.*, *36*, L03801, doi:10.1029/2008GL035586.
Ware, R., et al. (1996), GPS sounding of the atmosphere from low Earth orbit: Preliminary results, *Bull. Am. Meteorol. Soc.*, *77*(1), 19–40.
Wickert, J., et al. (2001), Atmosphere sounding by GPS radio occultation: First results from CHAMP, *Geophys. Res. Lett.*, *28*, 3263–3266, doi:10.1029/2001GL013117.
Wickert, J., T. Schmidt, G. Beyerle, R. Konig, and C. Reigber (2004), The radio occultation experiment aboard CHAMP: Operational data analysis and validation of vertical atmospheric profiles, *J. Meteorol. Soc. Jpn.*, *82*(1B), 381–395.
Wickert, J., et al. (2009), GPS radio occultation: Results from CHAMP, GRACE and FORMOSAT-3/COSMIC, *Terr. Atmos. Ocean Sci.*, *20*(1), 35–50.
Xie, F., J. S. Haase, and S. Syndergaard (2008), Profiling the atmosphere using the airborne GPS radio occultation technique: A sensitivity study, *IEEE Trans. Geosci. Remote Sens.*, *46*(11), 3424–3435.
Xu, X., J. Luo, and C. Shi (2009), Comparison of COSMIC radio occultation refractivity profiles with radiosonde measurements, *Adv. Atmos. Sci.*, *26*(6), 1137–1145, doi:10.1007/s00376-009-8066-y.
Zou, X., F. Vandenberghe, B. Wang, M. E. Gorbunov, Y. H. Kuo, S. Sokolovskiy, J. C. Chang, J. G. Sela, and R. A. Anthes (1999), A ray-tracing operator and its adjoint for the use of GPS/MET refraction angle measurements, *J. Geophys. Res.*, *104*, 22,301–22,318, doi:10.1029/1999JD900450.
Zuffada, C., G. Hajj, and E. R. Kursinski (1999), A novel approach to atmospheric profiling with a mountain-based or airborne GPS receiver, *J. Geophys. Res.*, *104*, 24,435–24,447, doi:10.1029/1999JD900766.
Zus, F., G. Beyerle, S. Heise, T. Schmidt, J. Wickert, and C. Marquardt (2011), Validation of refractivity profiles derived from GRAS raw-sampling data, *Atmos. Meas. Tech. Discuss.*, *4*(2), 1825–1852, doi:10.5194/amtd-4-1825-2011.